

Investigation of Endoscopic Techniques for Flow and Combustion Measurements

Min Wook Kang

Thesis submitted to the faculty of the Virginia Polytechnic Institute and State University
in partial fulfillment of the requirements for the degree of

Master of Science
In
Mechanical Engineering

Lin Ma – Chair
Srinath Ekkad
Wing Ng

April 18, 2014

Blacksburg, VA

Keywords: Combustion diagnostics, tomography, fiber, endoscopes

Investigation of Endoscopic Techniques for Flow and Combustion Measurements

Min Wook Kang

ABSTRACT

This work investigated the application of fiber-based endoscopes (FBEs) in combustion and flow measurements, especially for multidimensional and quantitative measurements. The use of FBEs offers several unique advantages to greatly reduce the implementation difficulty and cost of optical diagnostics. However, the use of FBEs requires registering the locations and orientations of the FBEs carefully for quantitative measurements, and degrades the spatial resolution of the images transmitted. Hence this work conducted a series of controlled tests to quantify the accuracy of the view registration process and the spatial resolution degradation for FBEs. The results show that, under the conditions tested in this work, the view registration process can be accurate within $\pm 0.5^\circ$ and the FBEs can resolve spatial features on the order of 0.25 mm. The combined effects of such view registration uncertainty and spatial resolution degradation are reflected in the re-projection error, which was shown to be within ± 0.5 pixels under typical conditions used in this work. Finally, based on these understanding, experiments were conducted to obtain instantaneous measurements of flame structures at kHz temporal resolution using FBEs, demonstrating the capability of resolving flame features on the order of 0.2~0.3 mm in three-dimensional.

ACKNOWLEDGEMENT

First of all, I take this opportunity to thank my advisory committee members, Drs. Lin Ma, Srinath Ekkad, and Wing Ng for their support and attention throughout this work. I would especially like to give sincere appreciation to my advisor, Dr. Lin Ma, whose guidance has enriched my education and increased my confidence as much as a degree ever could.

I would also like to offer my thanks to my colleagues in the Laser Diagnostic Lab, Xuesong Li, Tim Wu, AJ Wickersham, Qingchun Lei, and Frank He, for supporting my research project. Without their willingness to devote their valuable time, this project could not have been accomplished. My family and friends also deserve a great deal of my gratitude for their support, especially my fiancé Ellie. I would not be able to pursue this degree without her constant encouragement and support.

And most importantly, I thank God for all blessings and allowing me to stand where I am now. Please let my life be humble and be spent for you, Lord.

TABLE OF CONTENTS

ABSTRACT.....	ii
ACKNOWLEDGEMENT	iii
TABLE OF CONTENTS.....	iv
LIST OF FIGURES	v
LIST OF TABLES	vi
CHAPTER 1 : INTRODUCTION	1
CHAPTER 2 : CALIBRATION OF FIBER BASED ENDOSCOPES	5
2.1 View Registration Method	5
2.1.1. Intrinsic Parameters	7
2.1.2 Extrinsic Parameters	9
2.1.3 View Registration Method.....	9
2.2 View Registration Results.....	10
2.2.1 Experimental Arrangement.....	11
2.2.2 Validation Results.....	13
2.3 Spatial Resolution of FBEs	16
2.3.1 Experimental Setup.....	16
2.3.2 Spatial Resolution Results	18
CHAPTER 3 : DEMONSTRATION OF FLAME MEASUREMENTS	24
3.1 Experimental Setup and Formulation of 3D Tomography.....	24
3.1.1 Experimental Setup.....	24
3.1.2 Formulation of 3D Tomography.....	27
3.2 Premixed CH ₄ -O ₂ Cone-Flame	29
3.3 Premixed CH ₄ -O ₂ V-Flame	33
3.4 Premixed C ₃ H ₈ -O ₂ V-Flame.....	36
CHAPTER 4 : SUMMARY AND CONCLUSION	40
Reference	42
Appendix A: Distances and Orientations of FBE inputs	47

LIST OF FIGURES

Figure 2.1. Illustration of the view registration method.....	6
Figure 2.2. Schematic plot of view registration validation experiment.....	12
Figure 2.3. Example calibration results showing the projection of 3D world coordinates.....	14
Figure 2.4. Accuracy of the calibration results in terms of $\Delta\theta_x$ when $\Delta\varphi_y = 0^\circ$	15
Figure 2.5. Accuracy of the stereo calibration results in terms of $\Delta\varphi_y$ when $\Delta\theta_x = 20.13^\circ$	15
Figure 2.6. A photograph of a customized FBE bundle with four inputs and one output.....	17
Figure 2.7. Images of test chart obtained (a) without FBE, and (b) with a FBE.....	18
Figure 2.8. Image of the test chart along the x direction obtained directly with camera.....	19
Figure 2.9. Comparison of the image along the x direction.....	20
Figure 2.10. A scatter plot of the re-projection error.....	22
Figure 2.11. Histogram of the re-projection error in the x and y directions.....	23
Figure 3.1. (a) Schematic of the experiment setup. (b) a FBE input and coordinate system.....	25
Figure 3.2. A photograph of the experimental set up with 10 FEBs.....	26
Figure 3.3. (a) Photograph of CH ₄ -O ₂ cone-flame. (b)-(d) Ten simultaneous projections.....	29
Figure 3.4. (a) 3D reconstruction of cone-flame. (b) 2D slice from the reconstruction.....	30
Figure 3.5. Comparison of the flame front thickness from photograph and 3D reconstruction...31	31
Figure 3.6. (a): Photograph of CH ₄ -O ₂ V-flame. (b)-(d): Ten simultaneous projections.....	33
Figure 3.7. (a) 3D reconstruction of the V-flame. (b) 2D slices from the reconstruction.....	34
Figure 3.8. A cross-sectional view at $x = 0$ with flame contours from view 6 overlaid on top...35	35
Figure 3.9. Comparison of measured and computed projection.....	36
Figure 3.10. Nine simultaneous projections of CH ₄ -O ₂ V-flame.....	37
Figure 3.11. (a) 3D reconstruction of the V-flame. (b) 2D slices from the reconstruction.....	38
Figure 3.12. (a) A cross-sectional view of the flame. (b) Measurement from FBE 4.....	39

LIST OF TABLES

Table 1. Distances and orientations of FBE inputs for premixed CH ₄ -O ₂ cone-flame.....	47
Table 2. Distances and orientations of FBE inputs for premixed CH ₄ -O ₂ V-flame.....	47
Table 3. Distances and orientations of FBE inputs for premixed C ₃ H ₈ -O ₂ V-flame.....	47

CHAPTER 1 : INTRODUCTION

Three-dimensional (3D) spatial structures and rapid temporal dynamics are inherent to turbulent flames. Combustion diagnostics that can resolve such 3D spatial structures with adequate temporal resolution have therefore been long desired [1, 2] for the validation and development of predictive combustion models. However, it is a tremendous challenge to develop and implement 3D diagnostic techniques both due to fundamental reasons (e.g., the multi-spatial and -temporal scales, and multi-species of interest) and also practical reasons (e.g., optical access, harsh environments, and hardware limit) [3-5].

Despite these challenges, continued advancement in laser, camera, fiber, and computing technologies has enabled the initial demonstration of several 3D diagnostics, which can be broadly divided into three categories. The first category of techniques obtains 3D measurements by rapidly scanning a 2D technique, such as Mie scattering [6, 7] or laser induced incandescence [8]. Such scanning can be implemented either by actually scanning one illumination laser sheet generated by a high repetition pulsed laser using a rotating mirror [6, 7], or by firing multiple illumination laser sheets at multiple spatial locations generated by multiple pulsed lasers [8] to improve measurement rate at the cost of additional laser equipment. The second category of techniques obtains 3D measurements volumetrically by performing a 3D tomography without scanning [9-13]. Techniques in this category use multiple cameras to obtain 2D projections of the 3D target fields from various view orientations, based on which a tomographic reconstruction is performed to obtain 3D measurements [14]. The third possible category of techniques involves holographic imaging, which have been limited to nonreactive flows so far [15] and thusly will not be further discussed here.

The first two categories of techniques reviewed have both fundamental differences (in terms of spatial resolution, temporal resolution, field of view, etc.) and practical differences (in terms of equipment cost, alignment difficulty, optical access, etc.). Existing results suggest that the scanning strategy, due to the need of scanning, suffers from a tradeoff between the measurement volume and the spatial resolution in the scanning direction (i.e., the step size of scanning), and also has limited temporal resolution and measurement simultaneity (unless multiple lasers are used) [16]. In contrast, the tomographic strategy has been demonstrated in relatively large measurement volumes on the order of $10 \times 10 \times 10$ cm to provide instantaneous measurements at kHz temporal resolution [11, 12, 17].

However, the tomographic strategy has its own limitations. First, the spatial resolution of tomographic measurements is not as well defined as in the scanning strategy, and depends on factors besides the illumination and imaging systems such as the tomographic reconstruction algorithm and the choice of the projection view angles [9, 18-20]. Second, the reconstruction quality improves as more projection measurements are captured [11, 20], motivating the use of more cameras to obtain more projection measurements while equipment investment is always an issue in practice [21-23]. Additionally, in such applications, the direct use of imaging camera is also often not feasible due to their requirement for line-of-sight in hardly accessible areas of combustor devices or unfriendly environments [4, 24]. A possible alternative option is to employ specially designed industrial cameras along with associated connectors and enclosures. Nevertheless, such option is expensive and still have limitations in the hostile environments typically encountered in combustion applications [25, 26].

An alternative solution, as investigated in this work, involves the use of fiber-based endoscopes (FBEs), fiber bundles that can transmit images. The use of FBEs has been

investigated [25, 27-30] in recent years as a possible diagnostic option to overcome the high cost and restrictive issues of the direct use of imaging cameras as mentioned above. These FBEs are flexible and bendable to transfer images from the observation positions to cameras without the need for direct line-of-sight. They also have relatively small footprint (those used in this work have a core diameter of 10 mm) compared to many imaging cameras. Furthermore, as demonstrated in this work, they enable the recording of images from multiple views simultaneously onto a single camera, which greatly facilitates the implementation and significantly reduce the hardware cost of multiple dimension measurements [9, 10, 30].

Based on these previous successful demonstrations, this work focuses on investigating the potential and limitations of FBEs for quantitative combustion measurements, especially three-dimensional (3D) combustion measurements. However, there are several key issues that have to be resolved in order to make the quantitative measurements, including the view registration of the multiple images transmitted by the FBEs, the degradation of spatial resolution during the transmission, the degradation of signal uniformity during the transmission, and the degradation of signal linearity during the transmission. This work focuses on the first two issues (the view registration and the degradation of spatial resolution), and other issues will be discussed in subsequent publications. View registration refers to the determination of the relative location and orientation between the object and each FBE. When multiple FBEs are applied to image the same object from various distances and orientations, view registration is the first step in the data analysis for the quantitative interpretation of the measurements provided by the FBEs. Degradation of spatial resolution refers to the fact that the spatial resolution of the image, after transmitted from the FBEs to the camera, is typically lower than that captured directly by the same camera.

In the rest of this paper, Chapter 2 will first describe the view registration method used to determine the location and orientation of FBE measurements (Section 2.1), followed by a description of the experimental setup and a report of the results obtained (Section 2.2). Then, the experimental calibration of the spatial resolution of FBEs (Section 2.3) will be discussed. With the view registration and spatial resolution results, Chapter 3 will describe a demonstration of instantaneous 3D flame measurements based on tomographic chemiluminescence using the measurements from multiple FBEs as inputs. Tomographic chemiluminescence of CH^* is performed here due to its simplicity (no laser required) and yet potential as a powerful diagnostic. Once spatial-resolution is enabled, chemiluminescence signal can be used to infer key flame properties that are extremely difficult to obtain otherwise, such as local equivalence ratio [31], local heat release [31, 32], auto-ignition [33], and flame topography for model validation [9, 34]. Furthermore, as to be elaborated in Section 3.1.2, the mathematical formulation and solution algorithm of the tomography problem is not restricted to chemiluminescence, hence the results reported in this work are also expected to be of relevance to other types of 3D tomography measurements. Sections 3.2 to 3.4 then reports demonstration measurements of instantaneous 3D flame structures in a variety of flames. Lastly, Chapter 4 summarizes the work.

CHAPTER 2 : CALIBRATION OF FIBER BASED ENDOSCOPES

2.1 View Registration Method

In this work, an open source MATLAB tool developed for the calibration of cameras [35] is adapted for the view registration of multiple FBEs. This section provides a description of the mathematical formulation of the view registration method, and Section 2.2 will describe the experimental setup to validate the method and report the validation results.

Mathematically, view registration is the process of determining the location and orientation parameters of FBEs in order to transform from a world coordinate system to the image coordinate system. The view registration process is accomplished by evaluating three sets of coordinates: the 3D world coordinates, the 3D coordinates of the FBEs, and the 2D image coordinates. The 3D world coordinates are first converted to 3D FBE coordinates by translation and rotation. Then, the 3D FBE coordinates are projected to the 2D image coordinates. Once the 2D coordinates of the image are obtained, they can be related back to the 3D world coordinates. Figure 2.1 illustrates these concepts by considering the transformation of an arbitrary point M in the measurement domain through a FBE onto a camera.

First, a 3D world coordinate system $O-XYZ$ is established as shown, and denotes the coordination of M in this system as (x, y, z) . Second, a coordinate system is also established on each of the FBEs as shown. Here the system on the first FBE is denoted as $O_{FBE}^1 - X_{FBE}^1 Y_{FBE}^1 Z_{FBE}^1$. The signal emitted at point M propagates through the FBE and is imaged on the camera at point M' as shown. To describe the position of M' on the camera, a third 2D image coordinate system, $O_I - X_I Y_I$, is established on the image chip as shown. In this example, let's denote the coordination of M' in the image coordinate system to be (x_I, y_I) . Once $O-XYZ$ is fixed, (x_I, y_I)

depends on the locations, orientations, and optical parameters of the FBEs and cameras, i.e., the relative relationship between the three coordinate systems. Therefore, the goal of the view registration analysis is to determine such relative relationships by measuring the projections (e.g., M') of a set of points with known coordination in the $O-XYZ$ system (e.g., M) in the measurement domain.

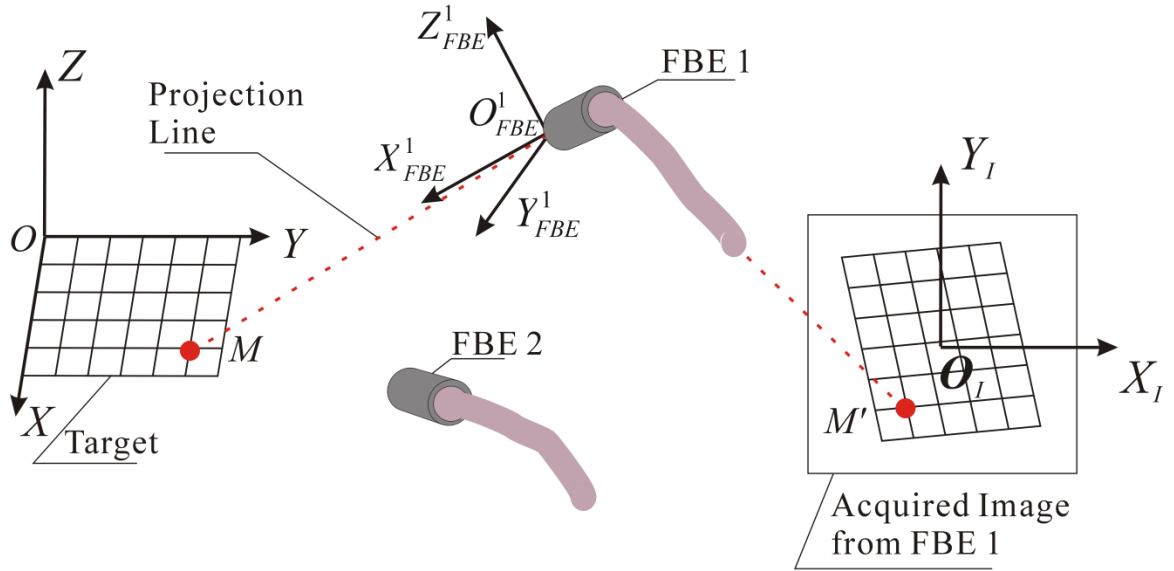


Figure 2.1. Illustration of the view registration method.

The transformation from the 3D world coordinates to the 3D FBE coordinates (e.g., from $O-XYZ$ to $O_{FBE}^1 - X_{FBE}^1 - Y_{FBE}^1 - Z_{FBE}^1$) is independent of the camera properties. Hence the parameters involved in this process are categorized as extrinsic parameters. These extrinsic parameters define the location and orientation of the FBEs in the 3D world coordinates (i.e., $O-XYZ$). When multiple FBEs are used, these extrinsic parameters, once obtained, can also be used to directly calculate the relative locations and orientations between any two FBEs. The transformation from the 3D world coordinates to the 3D FBE coordinates only involve rotation and translation

operations, and hence the extrinsic properties are quantified by a rotation matrix (R) and a translation vector (T), as to be detailed later.

The transformation from the 3D FBE coordinates to the 2D image coordinates is dependent on the properties of the cameras, and thus the parameters involved in this step are categorized as intrinsic parameters. The intrinsic parameters include the focal length vector (\bar{f}), principal point vector (\bar{c}), skew coefficient vector ($\bar{\alpha}$), and distortions vector (\bar{k}) of the lens system used on the camera. Both the extrinsic and intrinsic parameters are essential in order to quantify the transformation from the world coordinate system to the 2D image coordinates [35-38], as elaborated in sections 2.2.1 and 2.2.2 below.

2.1.1. Intrinsic Parameters

With the above understanding and definition of notations, here the view registration method is elaborated by analyzing the projection of M onto the 2D image as shown in Figure 2.1. We first illustrate the transformation from the 3D FBE coordinate system to the 2D image coordinate system by considering the projection of point M through an FBE, for example the first FBE. Denote the coordination of M in $O_{FBE}^1 - X_{FBE}^1 Y_{FBE}^1 Z_{FBE}^1$ to be $(x_{FBE}^1, y_{FBE}^1, z_{FBE}^1)$. As discussed above, the projection of point M onto the 2D image plane is dependent on the internal intrinsic parameters (i.e. $\bar{f}, \bar{c}, \bar{\alpha}$ and \bar{k}). In particular, \bar{f} is the 2×1 vector storing the focal length in pixels, c is the 2×1 vector storing the principal point coordinates, $\bar{\alpha}$ is the skew coefficient for the angle between x and y pixel axis, and \bar{k} is the 5×1 vector storing the image distortion coefficients for both radial and tangential distortions. Decentering or imperfect centering of the lens components and other manufacturing defects in a compound lens are common causes of

tangential distortions [39]. The projection of M starts with defining its normalized point coordinate (\bar{p}_n) as below without considering the lens distortion:

$$\bar{p}_n = \begin{bmatrix} x_{FBE}^1 / z_{FBE}^1 \\ y_{FBE}^1 / z_{FBE}^1 \end{bmatrix} = \begin{bmatrix} x_n \\ y_n \end{bmatrix} \quad (1)$$

Based on \bar{p}_n , the following projection vector \bar{p}_d is calculated to account for the effects of lens distortion:

$$\bar{p}_d = \begin{bmatrix} P_d(1) \\ P_d(2) \end{bmatrix} = (1 + k(1) \cdot r_n^2 + k(2) \cdot r_n^4 + k(5) \cdot r_n^6) \cdot \bar{p}_n + d\bar{p} \quad (2)$$

where $r_n^2 = x_n^2 + y_n^2$ and $d\bar{p}$ is the tangential distortion vector introduced by Duane [40]:

$$d\bar{p} = \begin{bmatrix} 2k(3) \cdot x_n \cdot y_n + k(4)(r_n^2 + 2x_n^2) \\ k(3)(r_n^2 + 2y_n^2) + 2k(4) \cdot x_n \cdot y_n \end{bmatrix} \quad (3)$$

On the other hand, the final pixel coordinates (x_l, y_l) of the projection of M on the 2D image plane is also related to \bar{p}_d via calculated by the following equation [35]:

$$\begin{bmatrix} x_l \\ y_l \end{bmatrix} = \begin{bmatrix} f(1) \cdot (p_d(1) + \alpha \cdot p_d(2)) + c(1) \\ f(2) \cdot p_d(2) + c(2) \end{bmatrix} \quad (4)$$

In summary, Equations (1) through (4) complete the transformation from the 3D FBE coordinate system to the 2D image coordinate system by relating $(x_{FBE}^1, y_{FBE}^1, z_{FBE}^1)$ and (x_l, y_l) . As seen from the above equations, this transformation depends on intrinsic parameters, i.e., $\bar{f}, \bar{c}, \bar{\alpha}$ and \bar{k} .

2.1.2 Extrinsic Parameters

After the above understanding of the transformation between the 3D FBE system and the 2D image system, here we discuss the transformation between the 3D world system and the 3D FBE system, which involves the extrinsic parameters. As mentioned above, the transformation between the 3D world coordinates and the 3D FBE coordinates involve rotation and translation operations, and hence the extrinsic properties are quantified by a 3×3 rotation matrix (R) and a 3×1 translation vector (T). When multiple FBEs are involved, there is an R matrix and T vector corresponding to each FBE. As an example, denote the rotation matrix and translation vector for the first FBE to be R_1 and T_1 , and then transformation of the coordination of point M (whose coordination is (x, y, z) in the O - XYZ system) is related to its coordination in the $O_{FBE}^1 - X_{FBE}^1 Y_{FBE}^1 Z_{FBE}^1$ (which is $(x_{FBE}^1, y_{FBE}^1, z_{FBE}^1)$) by the following equation:

$$\begin{bmatrix} x_{FBE}^1 \\ y_{FBE}^1 \\ z_{FBE}^1 \end{bmatrix} = \begin{bmatrix} x \\ y \\ z \end{bmatrix} \cdot R_1 + T_1 \quad (5)$$

2.1.3 View Registration Method

After establishing the transformation among the three coordinate systems as discussed above, here the view registration method is described. As illustrated in Equations (1) through (5), the projection of a point (e.g., M) from the world coordinates to the 2D image coordinates depends on both intrinsic and extrinsic parameters. Therefore, the goal of the view registration analysis is to determine these parameters by measuring the projections (e.g., M') of a set of points with known coordination in the O - XYZ system (e.g., M) in the measurement domain.

In this work, a calibration plate was fabricated with known patterns (a black and white chess board pattern for example) and installed with known position and orientation in the measurement domain, such the coordination of each point on the plate is known in the O - XYZ system (as shown in Figure 2.1). The images of the plate were taken by each FBE to be registered, and the experimental setup is schematically presented in Figure 2.2 in Section 2.2.1. The coordination of each point on the calibration was transformed into the image coordinate systems following Equations (1) through (5) by assuming a set of the intrinsic and extrinsic parameters. The projected images obtained from such calculation were then compared against the measured images to determine the intrinsic and extrinsic parameters iteratively. The pattern on the calibration plates, such as the locations of the intersection points between the white and black squares, facilitates the comparison between the calculated and measured images. If the calculated and measured images agree within a preset error limit, then the iteration was terminated and the view registration program output the assumed parameters as the results. Otherwise, an improved estimation of the parameters was obtained based on the initial guess, the degree of disagreement between the calculated and measured images, and the Jacobians of the equations involved in the transformation. The improved estimation is then used in the subsequent iteration.

2.2 View Registration Results

After the above discussion of the view registration method, this section describes the design of an experiment to validate the method and reports the validation results. The results

obtained in these experimental tests show that view angles of multiple FBEs can be registered with an accuracy of $\pm 0.5^\circ$.

2.2.1 Experimental Arrangement

Figure 2.2 shows the experimental setup schematically. A calibration plate with chess-board patterns (evenly spaced black and white squares of size $6\text{ mm} \times 6\text{ mm}$) was used as the registration target, in the place of the actual flame or flow to be measured. The plate was fixed on a rotational stage, so that the orientation of the plate relative to the 3D world coordinate system (O - XYZ) can be adjusted in a controlled way. This orientation was quantified by $\Delta\varphi_y$, the angle formed between calibration plate and the O - XY plane. In these experiments, the angle $\Delta\varphi_y$ can be adjusted and measured by a digital level from -15° to 15° with an accuracy of 0.1 degree. Both the calibration plate and the rotational stage were fixed on an optical bench. Two FBEs and their corresponding lenses were mounted on a solid aluminum optical breadboard, which was fixed perpendicular to the same optical bench as the calibration plate. As shown, one of the FBE and its corresponding lens were mounted on a rotational and translational stage, so that the position and orientation of this FEB relative to calibration plate and the other FBE can be adjusted in a controlled manner. The relative angle between the two FBEs was quantified by $\Delta\theta_x$ as shown in the figure, and experimentally, $\Delta\theta_x$ was determined by the readings on rotation mount which had an accuracy of 0.05 degrees.

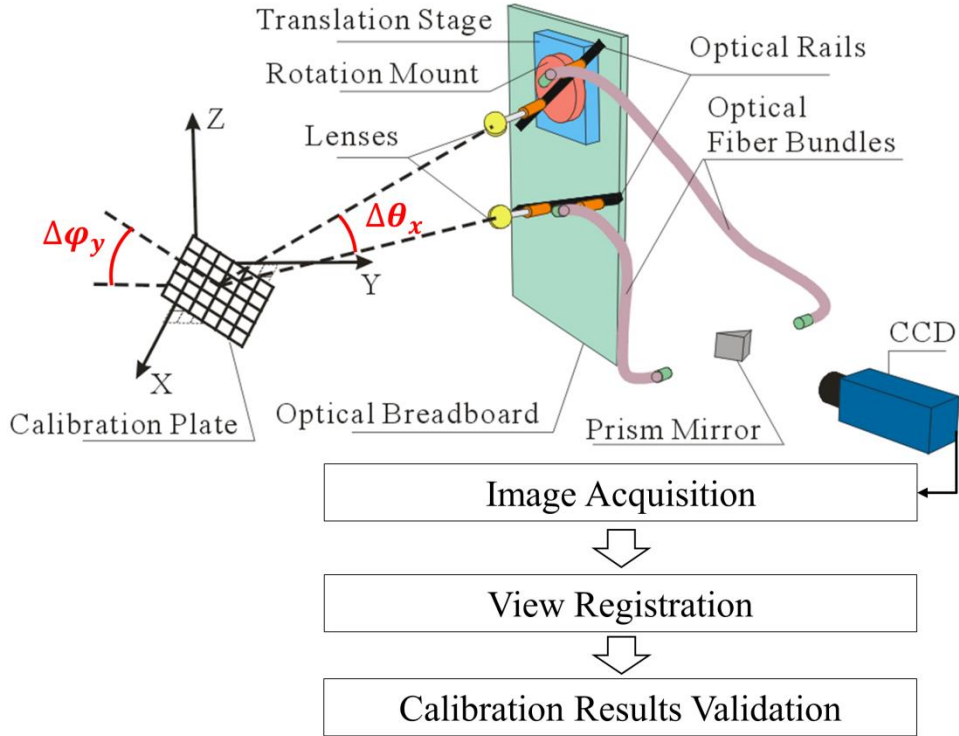


Figure 2.2. Schematic plot of view registration validation experiment.

Each of the FBEs consisted of an array of 350×350 individual single mode fibers, resulting in a total of 122,500 image elements per FBE. Each individual fiber, or image element, has a $17 \mu\text{m}$ core diameters and the overall length of the FBE is 1.35 m. To simplify the hardware and demonstrate the recording of multiple FBEs images on the same camera, a right-angle prism mirror was used to combine the output from both FBEs onto the same CCD camera (SensiCam with 1376×1040 pixels and pixel size of $6.45 \mu\text{m}^2$). The prism mirror had reflective coatings on both of its surfaces, and provided a clear aperture extending across its 90° angle between the coated surfaces. A set of lenses was used in front of input of the FBEs and also on the CCD camera, and these lenses were designed in such a way that the signal from each individual fiber in the FBE was approximately collected by one pixel on the CCD camera, resulting in an approximate one to one correspondence between the image element of the FBE

and the pixel of the CCD. The combined images from both FBEs were then acquired by the CCD camera at various angles of $\Delta\theta_x$ and $\Delta\phi_y$. These images were then analyzed by the view registration algorithm described above to output the location and orientation of the FBEs. Two of the outputs from the view registration analysis were $\Delta\theta_x$ and $\Delta\phi_y$, which then can be compared to their experimentally measured value as discussed above to validate the view registration algorithm.

2.2.2 Validation Results

Figure 2.3a shows a set of example calibration results for projecting the 3D world coordinates in the object domain (in this case, the calibration target) through a FBE onto a camera. And, the image shown is acquired by a camera. The crosses in the circles represent the detected intersection points of white and black squares from the image. The pattern of the white and black squares was known *a priori* and was used as input for the calibration method. The circles represent the re-projection of the same intersection points determined from the computed calibration parameters (output). The difference between each red cross and yellow circle thus represents the re-projection error. The re-projection error is typically less than two pixels, as shown in Figure 2.3b (which zooms in on the boxed region in Figure 2.3a). For the region shown in Figure 2.3b, the re-projection error was 0.6 pixels in both the x and y direction. Figure 2.3a does not faithfully visualize the re-projection error because of its scaling and resolution. The re-projection error depends on errors in the view registration process and also other factors such as the degradation of the spatial resolution, and will be discussed in more details in Section 2.3.

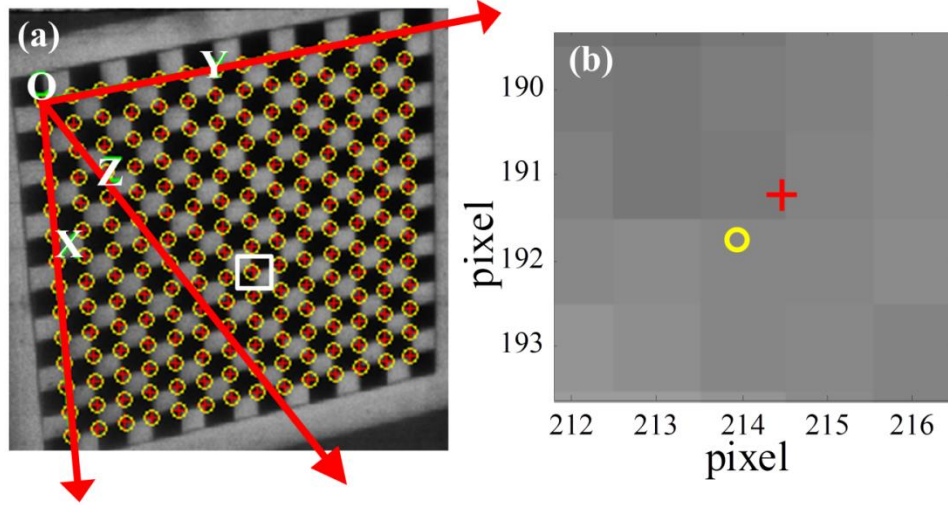


Figure 2.3. (a) Example calibration results obtained with a calibration plate. (b) A close view of a re-projection error in the boxed region from panel (a)

To validate the view registration method, Figure 2.4 and Figure 2.5 compare the angles measured experimentally versus those computed by our view registration program. Figure 2.4 compares $\Delta\theta_x$ (the angle between two FBEs) measured using the rotational mount discussed in Section 2.2.1 versus the computed value when $\Delta\varphi_y = 0^\circ$. Figure 2.4a shows the $\Delta\theta_x$ computed values when the relative orientations of the FBEs were adjusted, and the straight dashed line is a 45° line showing where the computed values would ideally match with the measured values. Figure 2.4b shows the residual of these results, defined as the difference between the measured value and the ideal match as shown in Figure 2.4a. As seen, the residual is within $\pm 0.5^\circ$ for this set of validation experiments.

Figure 2.5 shows another set of validation results in terms of $\Delta\varphi_y$ while $\Delta\theta_x$ is fixed at 20.13° . In this case, the angle $\Delta\varphi_y$ was adjusted and its value measured experimentally with the digital level as discussed in Section 2.2.1. Figure 2.5a compares the measured values with those computed from the view registration program. Similar to Figure 2.4, the dashed straight line in Figure 2.5a again illustrates the ideal match, and Figure 2.5b shows the residual of these results

which all fell in the range of 0.2 to 0.6⁰. Measurements were also performed under other conditions with different ranges of $\Delta\theta_x$ and $\Delta\varphi_y$, and the residual between the computed and measured values consistently remained within $\pm 0.5^0$, proving the accuracy of the view registration algorithm is acceptable.

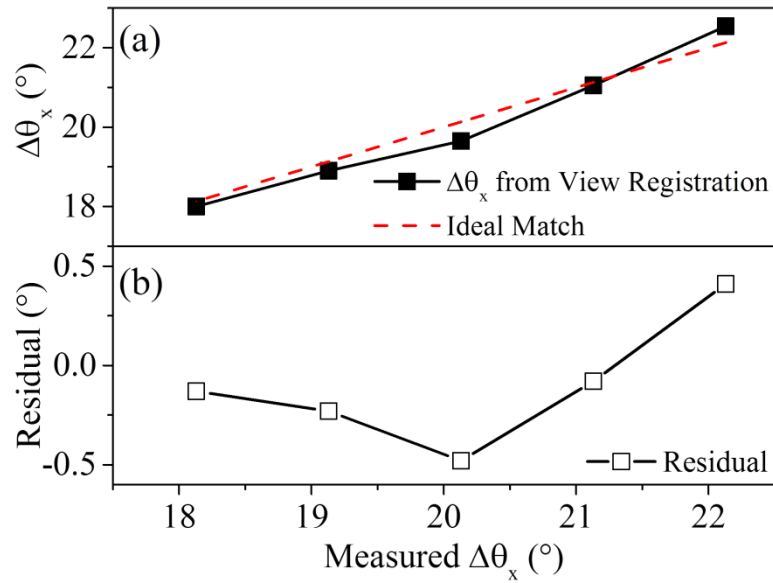


Figure 2.4. Accuracy of the calibration results in terms of $\Delta\theta_x$ when $\Delta\varphi_y = 0^\circ$.

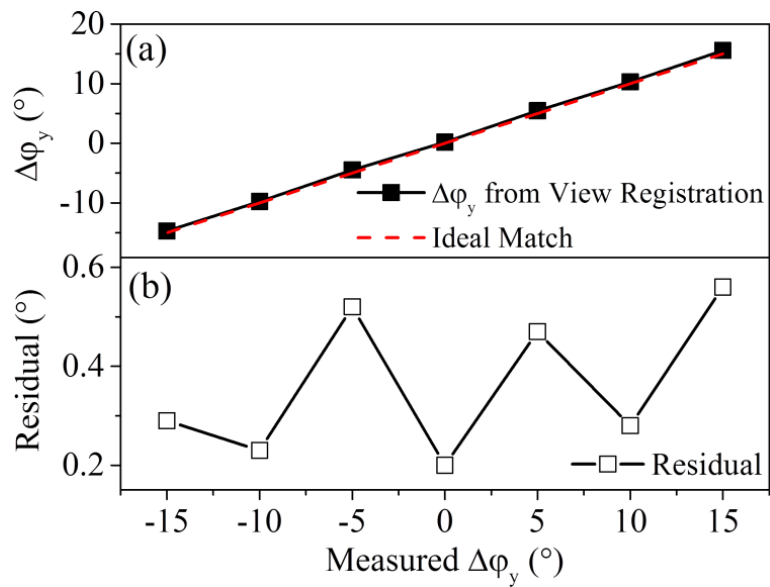


Figure 2.5 Accuracy of the stereo calibration results in terms of $\Delta\varphi_y$ when $\Delta\theta_x = 20.13^\circ$.

2.3 Spatial Resolution of FBEs

This section studies the spatial resolution of the images transmitted through the FBEs. The spatial resolution defines how sharply features in an image can be resolved and is one of the key aspects for imaging measurements in flows and flames. Optical fiber bundles are known to degrade and distort images. Therefore, this section describes our work to quantify the spatial resolution of images transmitted by FBEs considering degradation and distortion. The results show that with proper imaging lenses, sub-millimeter spatial resolution is possible with FBEs; and with the view registration methods described in Section 2.1, distortion can be accounted for with an accuracy of ± 2 pixels in the operation range tested in this work.

2.3.1 Experimental Setup

The experimental setup used here was similar to that depicted in Figure 2.2 for the validation of the view registration method, with two modifications. These modifications were primarily designed to quantify the study of spatial resolution (instead of view registration).

The first modification was that a resolution test chart (SilverFast USAF 1951) was used to replace the calibration plate used in the view registration test. The test chart consisted of patterns with size and spacing ranging from 0.78 to 2,000 micrometers, which were used to quantify the spatial resolution and image distortion. Since the test chart is transparent, a uniform light source (Gamma Scientific RS-5) was used to illuminate the test chart during the measurements. In the range used in this test, this uniform light source illuminated the test chart with a spatial uniformity better than 1% and a linearity deviation better than 0.25% RMS (root mean square).

The second modification was that in addition to the two FBEs used in the view registration test, we also used a new set of FBEs for the test of spatial resolution. One of the new FBE is shown in Figure 2.6.

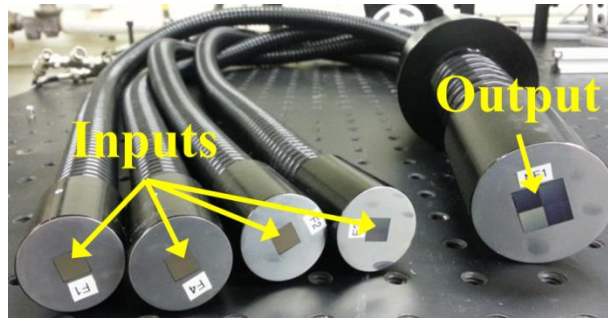


Figure 2.6. A photograph of a customized FBE bundle with four inputs and one output.

This new FBE is customized to have four input bundles as shown and all four input bundles were combined into one output head. The purpose of this customized FBE bundle is to allow the register of four images from the four input bundles on one camera chip without the need of additional optics (e.g., the prism mirror used in Figure 2.2). One such measurement is shown in Figure 2.7b. The FBE bundle shown in Figure 2.6 has an overall length of 2 m and a diameter of 2 cm, which were similar to those used in Figure 2.2 for the study of view registration. However, the new FBE has an array of 470×470 single mode optical fibers in each input bundle, resulting in a total of 883,600 ($470 \times 470 \times 4$) imaging elements from the output end. The view registration of the new FBEs was studied using the setup shown in Figure 2.2 (with two input bundles at a time), and results with the same accuracy were obtained as those described in Section 3.2.

2.3.2 Spatial Resolution Results

Figure 2.7 shows a set of images of the test chart with and without the use of FBE. Figure 2.7a shows the images acquired by the camera directly without the use of FBE, and Figure 2.7b shows the images of the test chart transmitted through four FBEs and captured by the same camera. The customized FBE bundle shown in Figure 2.6 were used to capture the image of the test chart from four different locations and orientations onto the same camera, so that the entire test chart was imaged from each view. As seen in Figure 2.7b, each view from each FBE on the camera occupied a region of about 400×400 pixels, again because the imaging optics were designed such that the signal from each individual fiber was projected approximately to one pixel.

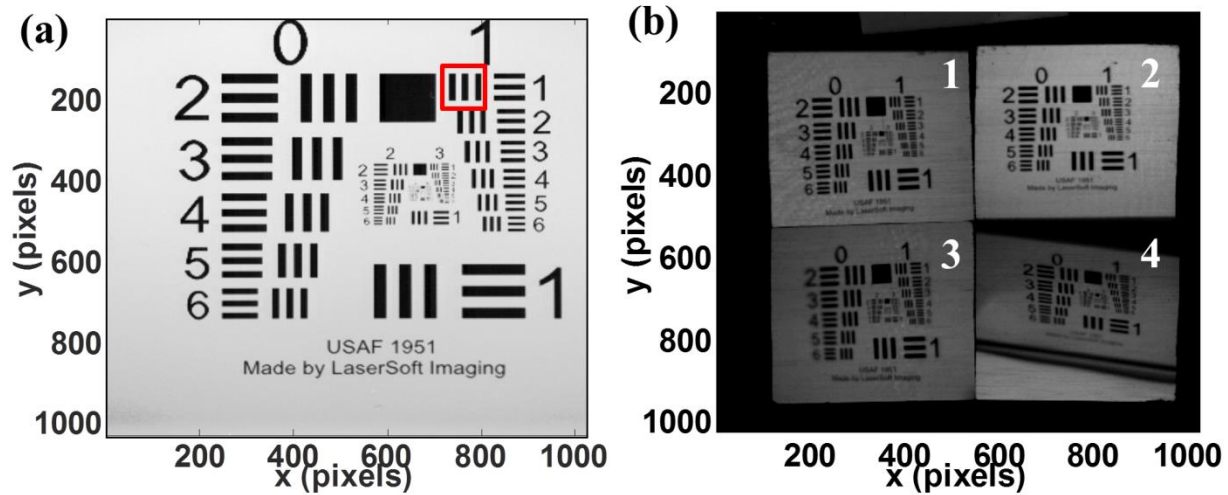


Figure 2.7. Images of test chart obtained (a) directly with camera without FBE, and (b) with FBE.

In this section, the spatial resolution in the sub-millimeter range is concerned the most. Therefore, here the boxed region on the test chart as shown in Figure 2.7a (i.e., Group 1-Element 1 on the test chart) is discussed. The pattern in this region consists of vertical black bars with a width of 0.25 mm separated from each other by 0.25 mm. Figure 2.8 shows the signal in Figure

2.7a, again captured directly with the camera, along the x direction, illustrating that the 0.25 mm feature can be sharply resolved.

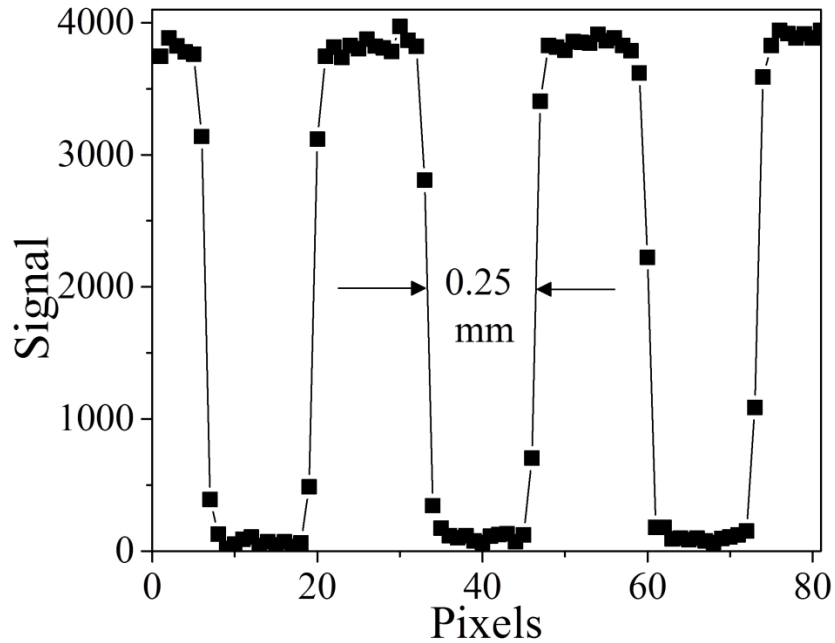


Figure 2.8. Image of the test chart along the x direction obtained directly with camera.

Figure 2.9 compares the measurements shown in Figure 2.8 (captured directly with the camera) with the measurements transmitted through a FBE to the camera. The data with FBE in Figure 2.9 are the same as those shown in Figure 2.8, and the data without FBE were taken from view 1 shown in Figure 2.7b by reading the image of Group 1-Element 1 pixel by pixel along the x direction.

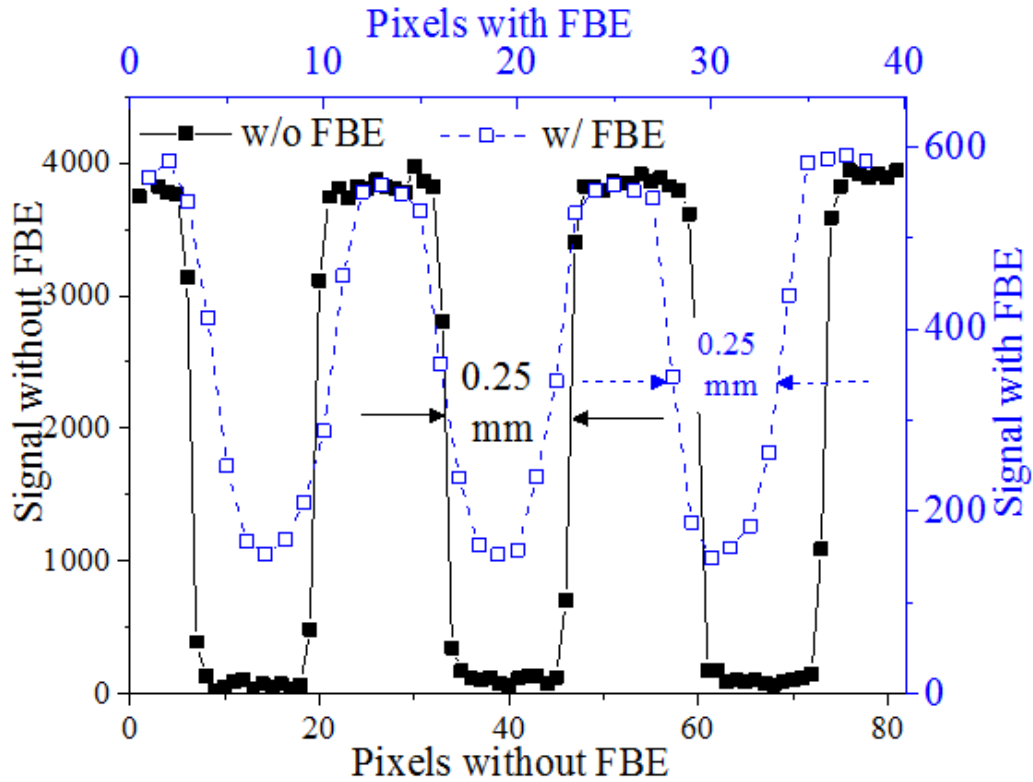


Figure 2.9. Comparison of the image along the x direction obtained without and with the use of FBE.

This comparison clearly illustrates that under the arrangement applied in these experiments, the spatial resolution of the images is degraded after transmission through the FBE. With the FBE, the vertical bars on the test chart were not resolved as sharply as without the FBE. Without the FBE, the signal rose and drop across one or two pixels on the edges of the bar; and in contrast, with the FBE, the signal rose and drop gradually. However, despite these issues, the image transmitted through the FBEs as shown still resolved the patterns on the test chart, and the full width at the half maximum of the signal corresponded to a physical dimension of 0.25 mm, the width of the black bars. Based on these results, Chapter 3 will discuss the application of the FBEs (together with the same imaging optics used here) to resolve flame features on the order 0.2 or 0.3 mm. In summary, two comments are noteworthy about these results. Firstly, note that

the achievable spatial resolution, either with the FBE or without, depends not only on the camera and the FBE but also the imaging optics and their placement. The imaging optics and their configuration used in these tests were specially designed to match those to be used in the subsequent flame measurements. Secondly, note that the comparison shown in Figure 2.7 and Figure 2.9 was designed such that the four views captured by four FBEs occupy the entire camera chip, and the image captured by the camera directly also occupy the entire camera chip. Essentially, the comparison was made under the assumption that the same number of pixels is available. This assumption reflects the practical design of the “best” imaging experiment with a fixed number of cameras.

The uncertainty in view registration as discussed in Section 2.2.2 and the degradation in spatial resolution as discussed above will cause error in the analysis of the image transmitted through the FBEs. In this work, the so-called re-projection error is used to quantify such error. As mentioned in Section 2.2.2, the re-projection error is defined as the difference between the image recreated using the parameters determined through the view registration process and the original image. Such quantification is facilitated by using test targets with known patterns like the chess board pattern shown in Figure 2.3 or the test chart shown in Figure 2.7. Because the captured images are used as inputs in the view registration process and the spatial resolution of the captured images is already degraded, the re-projection error represents a combined and overall error.

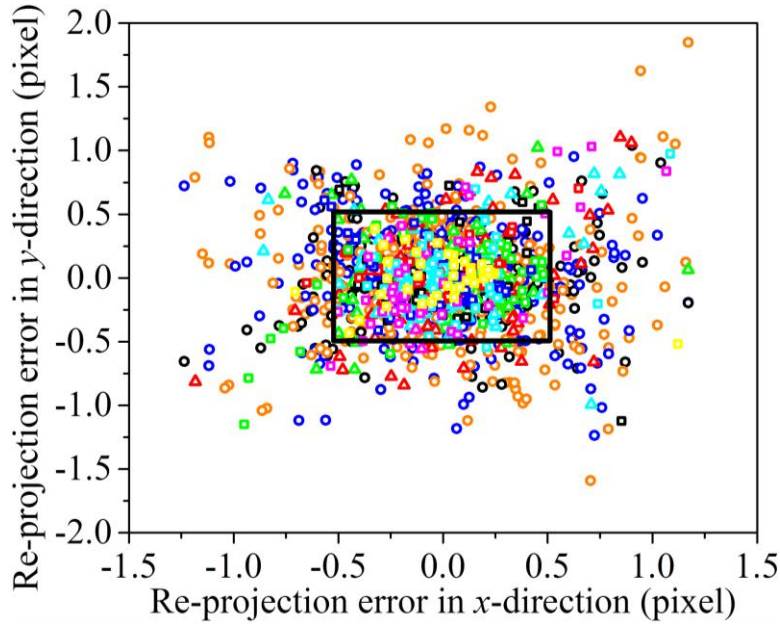


Figure 2.10. A scatter plot of re-projection error under various experimental conditions.

Figure 2.10 summarizes the re-projection errors for the tests performed in this study using the FBEs. Different symbols represent tests performed under different conditions (for example, under different $\Delta\theta_x$ and $\Delta\varphi_y$ values as described in Section 2.2.1, or using a different FBE, or using different test target). The re-projection error was determined by calculating the difference of a feature (such as the distance between the edges of a black bar) between its known value and the value obtained from the re-projected image. As shown in Figure 2.10, the re-projection errors in all these tests were within ± 1.25 pixels in the x direction and within ± 2.0 pixels in the y direction. The rectangular box in the center of Figure 2.10 illustrates the regime where error in both directions is within ± 0.5 pixel (e.g., 1 pixel of absolute error), which encompassed the dominant majority of the data points.

Figure 2.11 shows the histogram of the distribution of the re-projection error obtained from Figure 2.10, and confirms that the dominant majority ($\sim 94\%$) of the error occurs within ± 0.5 pixel in both the x and y directions. For the measurements performed here and to be

discussed in Chapter 3, each pixel corresponds to about 0.05 mm of physical size. Therefore, an absolute re-projection error of 1 pixel results in an uncertainty of 0.05 mm.

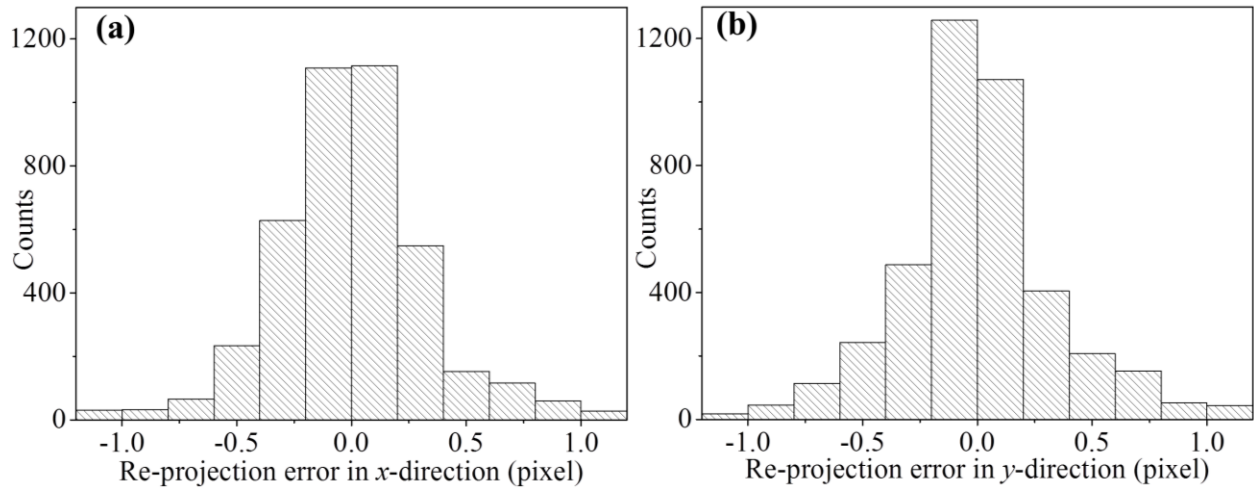


Figure 2.11. Histogram of the re-projection error in the x and y directions.

CHAPTER 3 : DEMONSTRATION OF FLAME MEASUREMENTS

Equipped with an understanding of the view registration, spatial resolution, and the error involved in these processes as discussed in Chapter 2, this chapter describes demonstrations of instantaneous 3D flame measurements based on FBEs. The measurements of 1) a premixed $\text{CH}_4\text{-O}_2$ cone-flame, 2) a premixed $\text{CH}_4\text{-O}_2$ V-flame, and 3) a premixed $\text{C}_3\text{H}_8\text{-O}_2$ V-flame are discussed in Section 3.2, 3.3, and 3.4, respectively. A total of 9 or 10 FBEs (10 FBEs for Section 3.2 and 3.3 and 9 FBEs for Section 3.4) were used to obtain projection measurements of these three different target flames from various orientations simultaneously. These projection measurements were recorded by three high speed CMOS cameras. Then, 3D tomographic reconstruction was performed based on the projection measurements to obtain 3D flame tomography. These results demonstrate that with FBEs, instantaneous 3D flame measurements can be obtained at kHz temporal resolution with mm spatial resolution or better, with manageable hardware and implementation.

3.1 Experimental Setup and Formulation of 3D Tomography

3.1.1 Experimental Setup

Figure 3.1 shows the general schematic of the demonstration experiments. Figure 3.1a shows the overall components and their layout in these experiments, and Figure 3.1b shows the details of a holder designed to align the FBEs and illustrates the coordinate systems.

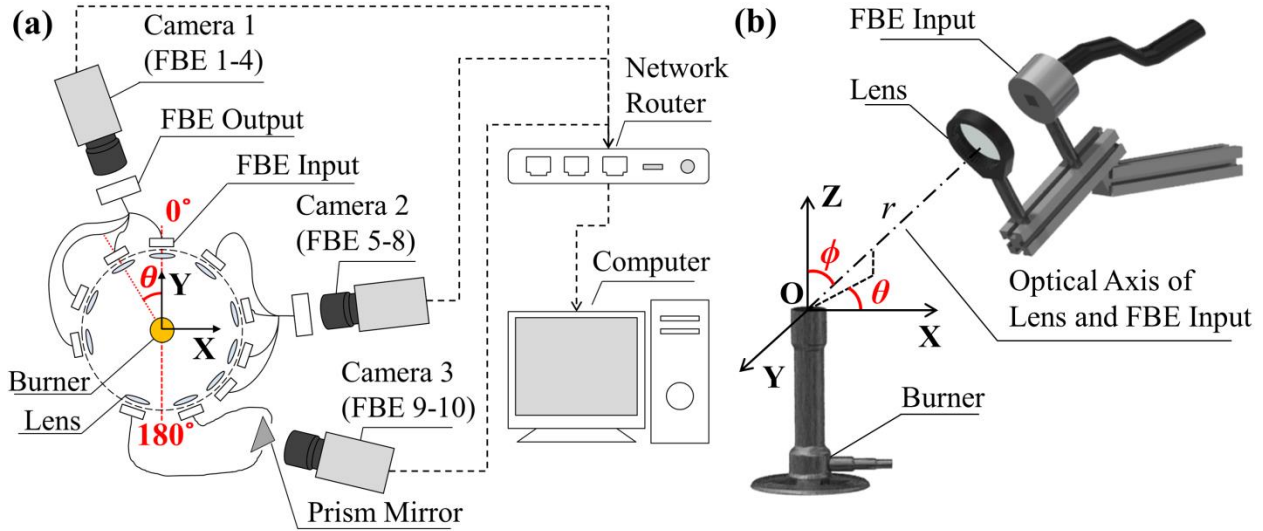


Figure 3.1. (a) Schematic of the experiment setup with 10 FBEs. (b) Illustration of the holder for FBE and the coordinate system using in tomography analysis.

The target flames were not stable, and therefore the projection measurements from various orientations were made simultaneously and instantaneously. The setup in Figure 3.1 used a total of three FBE bundles: two of them have four inputs as shown in Figure 2.6, and the third one has 2 inputs, whose outputs were combined using a prism mirror as shown previously in Figure 2.2. Therefore, a total of 10 FBEs and three CMOS cameras (Photron SA4 and SA6) were applied simultaneously as shown in Figure 3.1 to accomplish such projection measurements. In addition, a lens (51 mm and $f/1.0$) was used in front of each FBE input to gather more signals, and a lens (105 mm and $f/2.8$) was used on the camera. The projections measured by FBE 1 through 4 and 5 through 8 were captured on the first and second CMOS camera, respectively; and that measured by FBE 9 and 10 captured by the third CMOS camera. A photograph of the experimental setup with 10 FBE is presented in Figure 3.2 below.

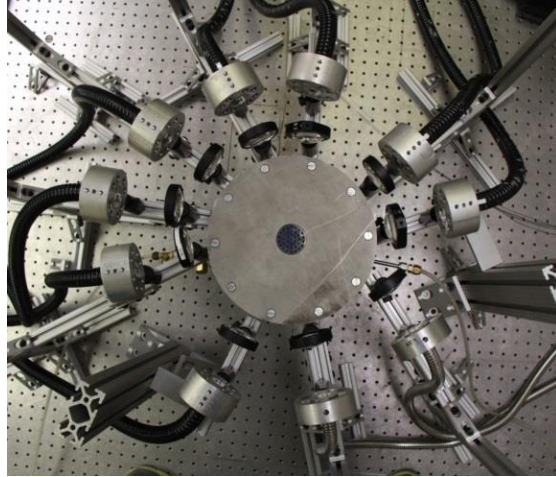


Figure 3.2. A photograph of the experimental set up with 10 FBEs.

For the setup with a total of 9 FBEs, FBE 10 is simply removed from the setup along with the prism mirror so that the projection from FBE 9 is directly measured with the third CMOS camera to avoid signal loss caused by prism mirror.

Figure 3.3 from following Section 3.2 shows a set of example projections taken by all the 10 FBEs and three cameras. In this measurement, the camera was set to a resolution of 1024×1024 pixels, a frame rate of 1 kHz, and an exposure time of 1 ms. Figure 3.3a is also provided to show a photograph of the same flame taken normal to its plane of symmetry for comparison purpose. As shown in Figure 3.1a, in these measurements, the 3D world coordinate system (O - XYZ) was defined in such a way that the X and Y -axes plane was located at the jet exit, the Z -axis was along the direction of the flow, and the origin O was fixed at the center of the jet exit. All the cameras were synchronized by a network router, and the control and data acquisition were centralized by a computer.

Figure 3.1b shows the details of a holder designed to align the FBEs and also further illustrates the coordinate systems as mentioned. The holder was customized in house, and the major component in the holder was an optical rail was use to align a lens with an FBE. After the

lens and FBE were aligned, the orientation and location of the lens and FBE combination can be defined by a distance (r) and two angles (θ and φ) as shown in Figure 3.1a and Figure 3.1b, where r specifies the distance between O and the center of the lens, θ specifies the angle formed by the optical axis of the lens-FBE combination relative to the Y axis, and φ specifies the angle formed by the optical axis of the lens-FBE combination relative to the Z axis. Note that the optical axis of the lens-FBE does not have to be aligned to pass O as shown in Figure 3.1b. Figure 3.1b shows it this way only to avoid clustering the plot. The description of the experimental setup illustrates the motivations for using FBEs for combustion and flow diagnostics. As seen, the FBEs are bendable therefore circumventing the need for direct-line-of-sight as required in the use of cameras. They allow the acquisition of measurements from multiple locations and views to be captured by a single camera. These features reduce the requirement on optical access, physical space, and hardware cost compared to tomographic implementation using cameras directly [11, 12, 41], which are all important considerations in practice. Furthermore, these features allow to facilitate the measurements from arbitrary view angles (rather than view angles dictated by line-of-sight or physical space), which have been shown to be advantageous to enhance the fidelity of tomographic reconstructions [18, 42].

3.1.2 Formulation of 3D Tomography

With the above definition of the coordinate system, the location and orientation of each FBE input (i.e., r , θ and φ) were determined using the view registration method as discussed in Section 2.1 before the flame measurements. As an example, Table 1 in Appendix A lists the values of r , θ and φ of the 10 flame projections shown in Figure 3.3 determined from the view registration method. In these experiments, the 3D imaging of flame topography is demonstrated

based on CH^* concentration. Denoted the 3D instantaneous concentration of CH^* as $F(x,y,z)$, and discretized F into cubic voxels in the O - XYZ coordinate system. The projection (P) of F obtained from a FBE is a 2D line-of-sight-integrated image of F on the camera. The relationship between P and F is shown in Equation (6) below:

$$P(r, \theta, \phi) = \sum_{x_i, y_i, z_i} F(x_i, y_i, z_i) \cdot PSF(x_i, y_i, z_i; r, \theta, \phi) \quad (6)$$

where x_i, y_i, z_i represent the voxel centered at (x_i, y_i, z_i) ; and PSF is the *point spread function* defined as the projection formed by a point-source located at (x_i, y_i, z_i) with unity intensity. Physically, Equation (6) states that the projection is a weighted summation of the PSF across all voxels, and the weights are the value of the sought distribution. The 3D tomographic problem is then formulated as:

$$\text{Given a set of projections } (P_s) \text{ measured at various of } r, \theta \text{ and } \phi, \text{ find } F(x,y,z). \quad (7)$$

Although this work focuses on the measurement of chemiluminescence from CH^* , the PSF does not depend on the specific physical processes involved (e.g., chemiluminescence, emission, or droplet scattering). The PSF only depends on the image system [43] and its position and orientation relative to O - XYZ . Therefore, Equations (6) and (7) can be applied to other types of optical tomography measurements based on other signal generation mechanisms, as being pursued in the ongoing work. Numerous algorithms [9, 11, 19, 44-46] have been proposed to solve Equation (7). An algorithm based on simulated annealing [9] (code named TISA, Tomographic Inversion by Simulated Annealing) is implemented for this work. The algorithm has been demonstrated to solve other types of inversion problems in combustion measurements [4, 47, 48]. Details and validation of the TISA algorithm are provided in [9, 20, 49].

3.2 Premixed CH₄-O₂ Cone-Flame

In this section, the demonstration of flame measurement is conducted on a premixed CH₄-O₂ cone-flame, which has relatively simple flame structure. The flow rates of CH₄ and O₂ are 2.0 and 2.3 SLPM, respectively, and the jet diameter is 2.5 mm, resulting in a Reynolds number of 1,980. As mentioned earlier, Figure 3.3b through Figure 3.3d shows 10 projection images from each FBE on the camera occupied a region of about 400×400 pixels as shown. Figure 3.3b through d are captured with the first, second and third camera respectively. The values of r , θ and φ of these 10 flame projections are obtained from view registration and listed in Table 1 (located in Appendix A).

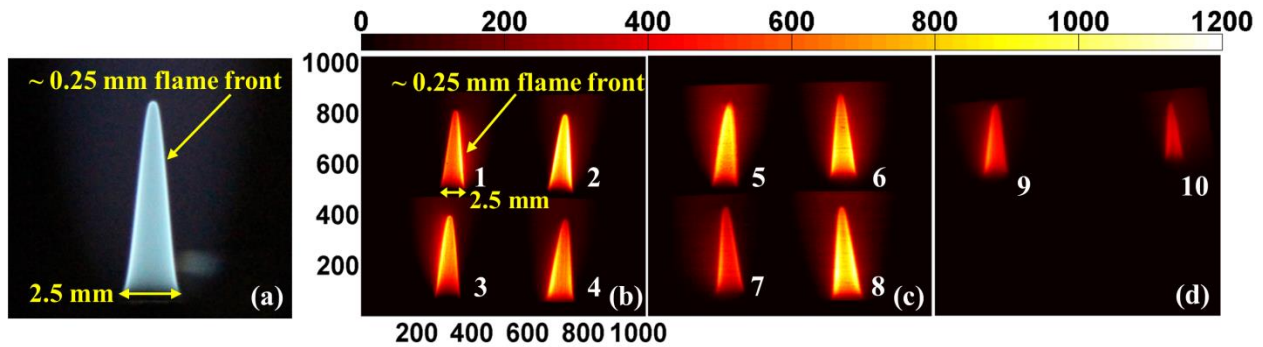


Figure 3.3 (a) Photograph of a premixed CH₄-O₂ cone-flame. (b)-(d) Ten simultaneous projections of a cone-flame captured on three cameras using three FBE bundles.

Using these 10 projections as inputs to the tomographic algorithm, a reconstruction of 3D instantaneous flame structure was performed and is shown in Figure 3.4. Figure 3.4a shows the 3D iso-surface with the highest CH* concentration, and Figure 3.4b shows a cross-sectional view of the CH* distribution based on the 3D reconstruction. The results illustrate the capability of FBEs for obtained 3D combustion measurements. First, note that even though the flame is axially symmetric, no *a priori* knowledge of such symmetry was assumed in the tomographic reconstruction and the problem was solved as a 3D problem. The volume imaged by the FBEs

was $\sim 30 \times 30 \times 30 \text{ mm}^3$. Dark regions of the imaged volume as seen on Figure 3.3b through Figure 3.3d where no flame was present were clipped before tomographic inversion to save computational cost. After the clipping, each projection is $\sim 400 \times 400$ pixels (resulting in a total of 1.6×10^6 equations in the form of Equation (6)), and an effective measurement volume of $6 \times 6 \times 12 \text{ mm}^3$ (as shown in Figure 3.4), which was then discretized into $100 \times 100 \times 50 (= 1 \times 10^6)$ voxels in the x , y , and z direction, respectively, for the tomographic inversion. 3D tomographic reconstruction as shown in Figure 3.4 is computationally intensive, involving a system of 1.6 million equations and 1 million unknowns, and the PSF at each view angle requires 3~4 GB of memory storage. Using the TISA algorithm, the reconstruction took ~ 4 hours to complete on a workstation with an Intel Xeon E5-2650 processor and 96 GB of memory.

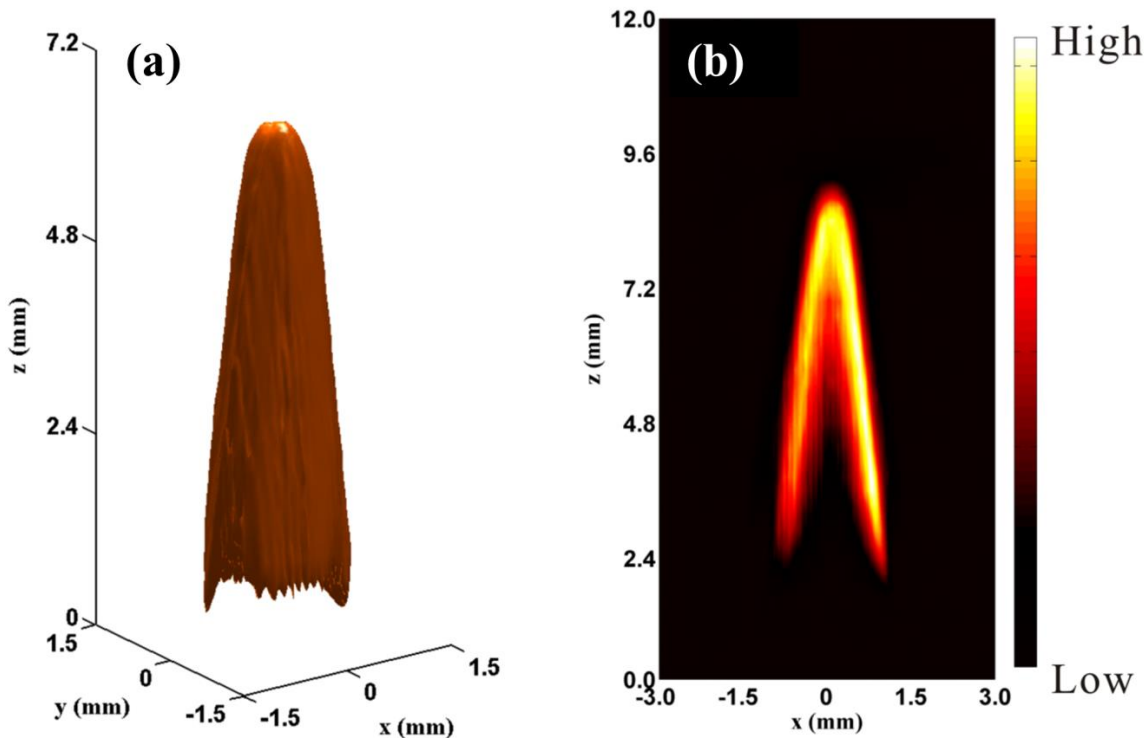


Figure 3.4. (a) 3D reconstruction of cone-flame. (b) A 2D slice to better illustrate the thickness of the flame front.

The flame topography, size, and location are all correctly reconstructed in the results shown in Figure 3.4 when compared to the photograph shown in Figure 3.3a, demonstrating the 3D measurement capability of tomography imaging using FBE at kHz rate. Figure 3.5 examines the results in more detail beyond the overall features of the flame. Figure 3.5 compares the flame front thickness obtained from photograph as shown in Figure 3.3a versus that obtained from the 3D tomographic reconstructions shown in Figure 3.4a at various flame heights. Because both Figure 3.3a and Figure 3.4a were based on chemiluminescence measurements, the thickness shown here is the reaction zone thickness [50]. The photograph presented in Figure 3.3a has a resolution of 0.023 mm/pixel and the thickness of the flame front was directly read based on the sharpest change in the brightness on the photo. The thickness of the flame was also read in the same way from the reconstruction, but four values were read at each flame height in orthogonal directions due to the availability of 3D information, and the average of these four values are plotted in Figure 3.5 with the error bar representing their standard deviation.

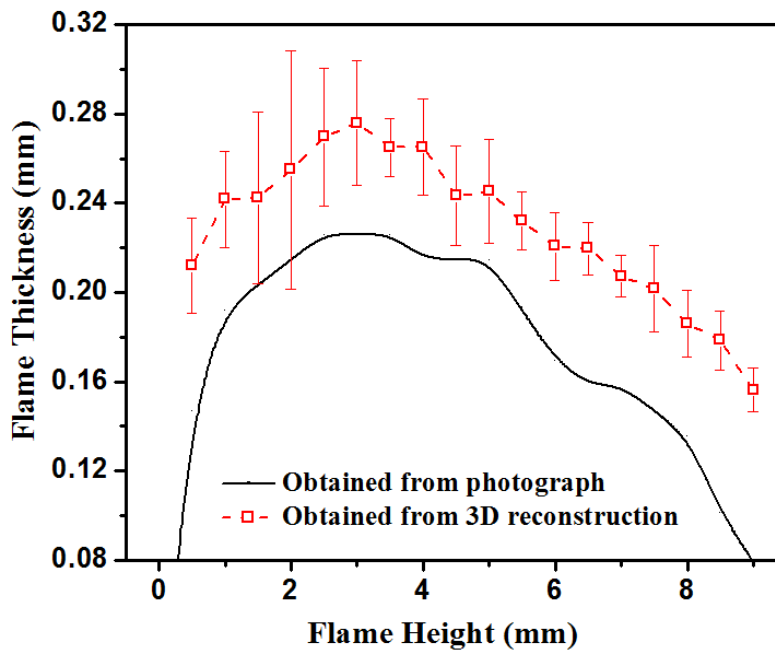


Figure 3.5 Comparison of the flame front thickness obtained from photograph and 3D tomographic reconstructions.

These results show that 1) the thickness determined from the 3D reconstruction is systematically larger than that determined from the photograph, 2) the four values read at each height from the 3D reconstruction have a non-negligible variation. However, the thickness determined by the 3D reconstruction 1) is in the correct range of ~ 0.06 mm, and 2) shows the correct trend of flame thickness at various flame height [50]. Therefore, these results in Figure 3.5 suggest both the fidelity and issues of the 3D measurements as demonstrated in this work. These results indicate tomographic techniques based on FBEs are able to resolve sub-mm spatial features in 3D with 10 views in a measurement volume of $6 \times 6 \times 12$ mm³, and the spatial resolution approximately scale linearly with respect to the size of the measurement volume and inversely with respect to the number of views [51].

Therefore, the results shown here provide experimental data to guide the estimation of spatial resolution of tomography techniques. The disagreement and variation observed in Figure 3.5 are due to several possible factors including discretization error, experimental uncertainty, and reconstruction error. As mentioned, the photograph is discretized to 0.023 mm/pixel and the 3D reconstruction to 0.06 (x and y direction) and 0.24 (z direction) mm/voxel. Such finite discretization was estimated cause $\sim 10\%$ and $\sim 20\%$ uncertainty in determining the flame thickness from the photograph and the 3D reconstruction, respectively. A finer discretization in the tomographic reconstruction will reduce such uncertainty (at the cost of increased computational and memory requirement as discussed earlier).

3.3 Premixed CH₄-O₂ V-Flame

After the above study on a simple cone-flame, Figure 3.6 shows another set of measurements on a more complicated premixed CH₄-O₂ V-flame, created by placing a rod (of a diameter of 3.175 mm) as a bluff body at the jet exit (of a diameter of 8 mm). In this experiment, the 3D world coordinate system (*O*-XYZ) was defined in such a way that the *X*-axis was perpendicular to the rod, the *Y*-axis was along the rod, the *Z*-axis was along the direction of the flow, and the origin *O* was fixed at the center of the jet exit. The values of *r*, *θ* and *φ* of these 10 flame projections are listed in Table 2 (located in Appendix A).

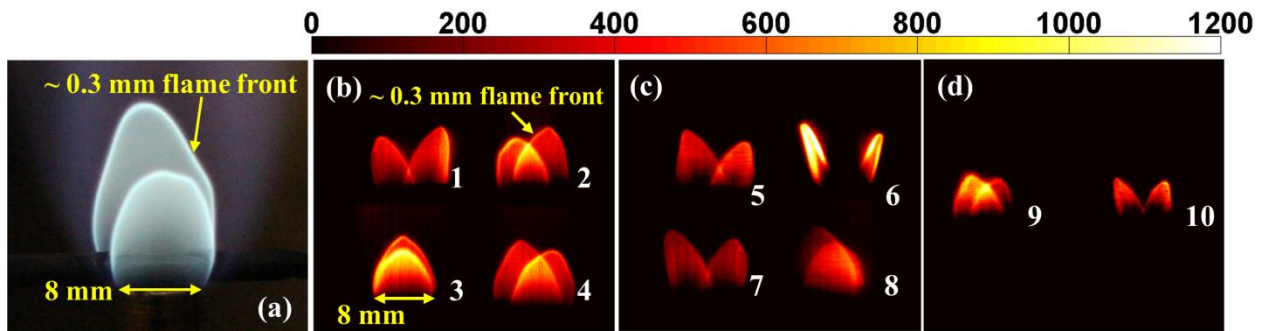


Figure 3.6 (a): Photograph of a premixed CH₄-O₂ V-flame. (b)-(d): Ten simultaneous projections captured on three cameras using three FBE bundles.

This V-flame exhibits two close-tip flame fronts that were overlapping on 9 projections. Figure 3.6a shows a photograph of the flame, and Figure 3.6b through Figure 3.6d show the 10 simultaneous projections measured by the FBEs and three cameras. The measurements were taken with 4.5 and 4.7 SLPM of CH₄ and O₂, respectively, resulting in a Reynolds number of 2,920. Due to the larger size of this flame compared to that used in Figure 3.3, the chemiluminescence emissions are stronger so that projection measurements can be taken at a

higher frame rate (2 kHz) and shorter exposure time (0.5 ms) with sufficient SNR. The resolution of all three cameras was 1024×1024 pixels as before.

The 3D reconstruction of the V-flame is performed using the 10 projections presented in Figure 3.6. The volume imaged by the FBEs was $\sim 15 \times 15 \times 15 \text{ mm}^3$. Again, the dark regions of the images were clipped, resulting in 400×400 pixels for each view and a total of 1.6×10^6 equations in the form of Equation (6). The overall dimension of the probed volume was $14 \times 14 \times 6 \text{ mm}^3$, and discretized into $140 \times 140 \times 30 (= 5.88 \times 10^5)$ voxels. Figure 3.7a shows a 3D iso-surface plot of the V-flame at the highest CH^* concentration. As a different way to view the 3D flames structures, Figure 3.7b shows 2D slices taken out of the reconstruction at three different x locations. The thickness of the flame fronts was estimated to be around 0.30 mm based on the line-of-sight chemiluminescence images, which was clearly resolved by the 3D reconstructions shown in Figure 3.7b.

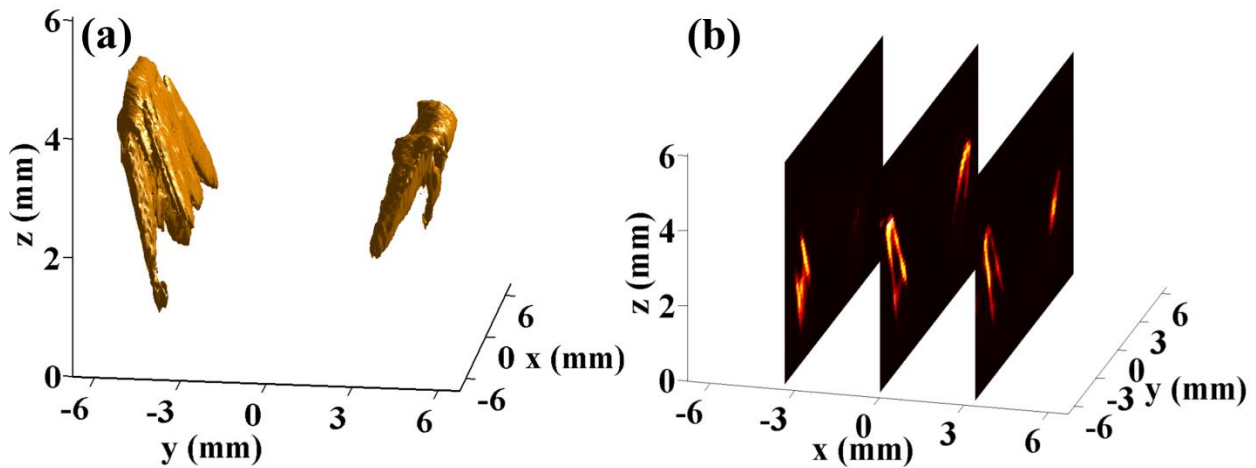


Figure 3.7. (a) 3D reconstruction of the V-flame. (b) 2D slices from the reconstruction at three different x locations

To facilitate the validation of the 3D reconstruction, the cross-sectional view in Figure 3.8 was chosen to be from the same orientation as the view 6 (the view from FBE 6) in Figure 3.6c. The flame contour determined from the view 6 in Figure 3.6c (shown as the white line) was overlaid on the cross-sectional view. As seen in Figure 3.8, the 3D reconstruction correctly captured the flame shape both quantitatively and qualitatively. For instance, the V-flame was not symmetric and the left branch of the V-flame was taller and stronger, which was correctly reconstructed; and the flame contour from the reconstruction agrees well with that taken from view 6 in Figure 3.6c.

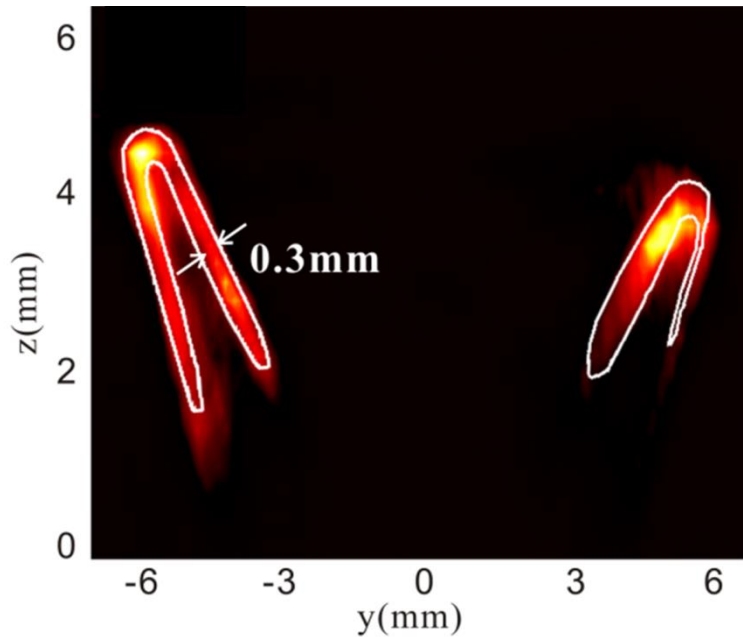


Figure 3.8. A cross-sectional view at $x=0$ with flame contours from view 6 overlaid on top.

Figure 3.9 compares the measured projections (views 1, 3, 5, and 6 shown in Figure 3.6b and Figure 3.6c) versus the projections computed from the 3D reconstruction shown in Figure 3.7a via ray tracing. As seen, the comparison shows that the computed projections agree with the measured projections both qualitatively and quantitatively, supporting the validity of the 3D measurements (not necessarily proving it).

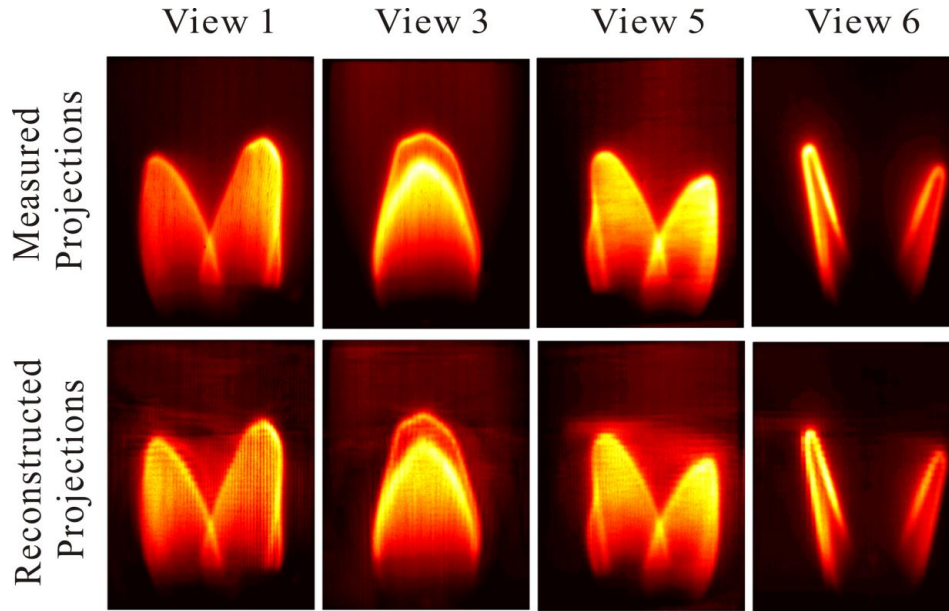


Figure 3.9. Comparison of measured and computed projections

3.4 Premixed $C_3H_8-O_2$ V-Flame

Lastly, Figure 3.10 shows a set of 3D measurements using the 9 FBEs on a premixed $C_3H_8-O_2$ flame. Similar to the CH_4-O_2 V-flame discussed above, this flame was also created by placing a 2mm rod as the stabilizing bluff body on a 5mm diameter jet. These 9 simultaneous projections of the target flame are taken with an exposure time of 0.5 ms and a frame rate of 2 kHz. Under such frame rate, the CMOS chip (Photron SA4) operates with 1024×1024 pixels and each projection is represented with 350×350 pixels, which features a resolution of 0.020 mm/pixel. Due to the different fuel and burner configuration, the flame exhibited open-tips and an overall V-shape with two flame fronts. The values of r , θ and φ of these 9 flame projections are listed in Table 3 (located in Appendix A).

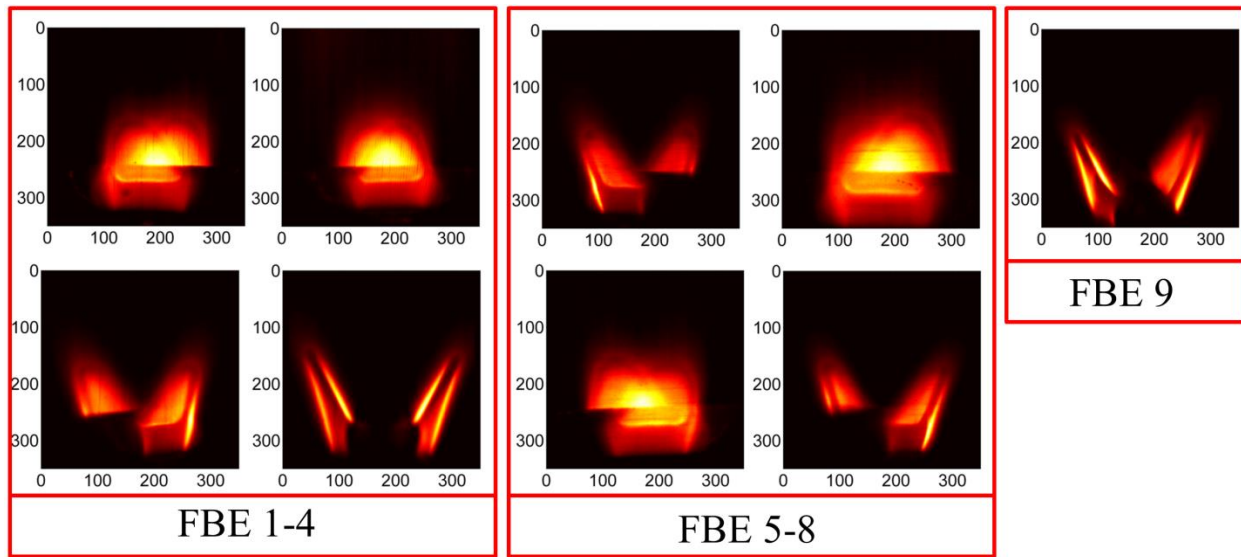


Figure 3.10. Nine simultaneous projections of a premixed $\text{CH}_4\text{-O}_2$ V-flame obtained using nine FBEs and three cameras

Using the 9 simultaneous projections shown in Figure 3.10, a 3D reconstruction was performed and the result is shown in Figure 3.11. Figure 3.11a shows the 3D iso-surface with the highest CH^* concentration obtained from the tomographic reconstruction to visualize the flame structures. And, Figure 3.11b shows 2D slices of the CH^* concentration from the reconstruction at three different x locations. After clipping the black regions, the effective measurement volume had a dimension of approximately $9.5 \times 5 \times 6 \text{ mm}^3$, as shown in Figure 3.11a.

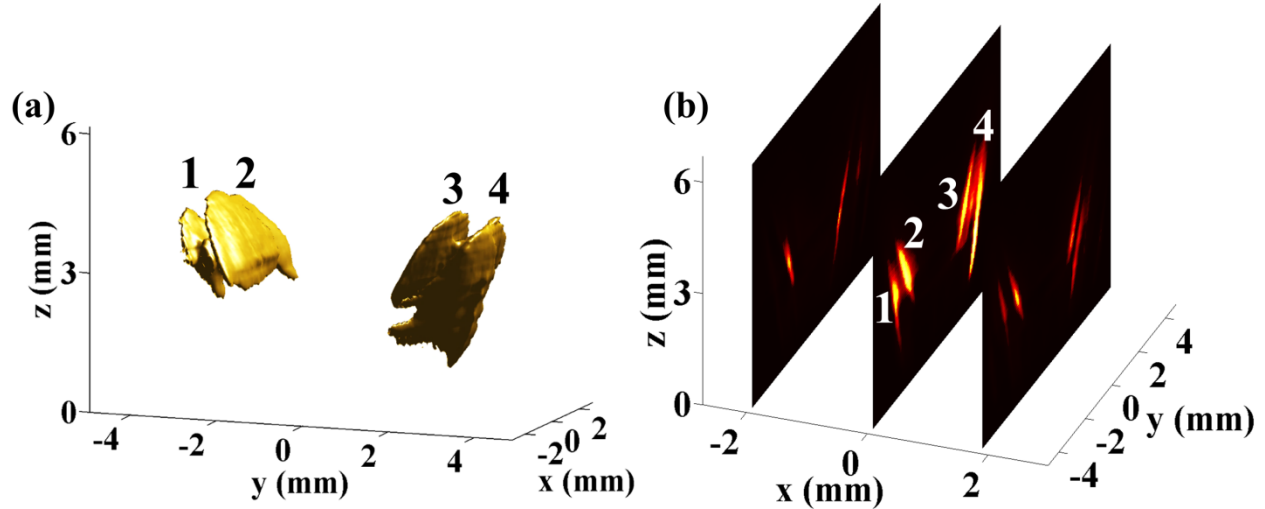


Figure 3.11. (a) 3D reconstruction of the V-flame. (b) 2D slices from the reconstruction at three different x locations

Due to the particular flame configuration (fuel, oxidizer, and stretch rate), the flame in these experiments exhibited open tips [50, 52]. The open-tip feature combined with the use of the rod created 4 distinct flame fronts, as seen from view provided by the FBE 4 as shown in Figure 3.10. The FBE 4 was aligned with $\theta=0^0$ and $\varphi=0^0$, therefore providing a view of flame precisely along the axial direction of the rod. The 3D reconstructions shown in Figure 3.11a captured all four flame fronts as labeled accurately, including the size and position of each flame front. Also, the thickness of each flame front was estimated to be 0.25 mm based on the axial view provided by the FBE 4 as shown in Figure 3.10, and the all the flame fronts were resolved as shown in Figure 3.11, consistent with the validation of the FBE's ability to resolves features on the order of 0.25 mm in Section 2.3.

To better illustrate the spatial resolution of the 3D reconstruction using the FBEs, Figure 3.12 compares the flame fronts determined from the 3D reconstruction against those determined by the traditional line-of-sight chemiluminescence measurements. Figure 3.12a shows a cross-sectional view of the 3D reconstruction along the central plane (i.e., the plane at $y = 0$), again

clearly displaying the four flame fronts obtained from the 3D tomographic reconstruction. To compare the flame fronts determined by the 3D reconstruction against those determined by traditional line-of-sight chemiluminescence, Figure 3.12b overlays the contours of the flame front (shown as black line) determined from Figure 3.12a on top of the flame projection from the FBE 4 as shown in Figure 3.10. This comparison shows that the 3D reconstruction based on FBE measurements correctly captured the shape and size of the flame both qualitatively and quantitatively, demonstrating the feasibility of using FBEs for instantaneous and high-speed imaging measurements. Additionally, as compared to the close-tip feature of the methane-oxygen flame shown in Figure 3.7, the results shown in Figure 3.11 clearly resolved the open-tip feature of the propane-oxygen flame. These results demonstrate the FBE's usefulness for resolving sub-millimeter flame features, as illustrated by resolving the flame fronts and also by resolving the open- and close-tip features of different flames.

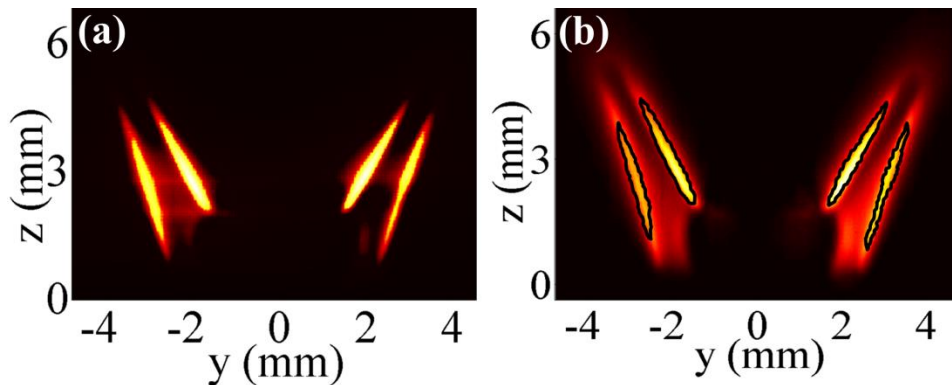


Figure 3.12. (a) A cross-sectional view of the flame at $x = 0$ mm obtained from the reconstruction. (b) Flame contours determined from panel (a) overlaid on top of the line-of-sight chemiluminescence measurements obtained by FBE 4.

CHAPTER 4 : SUMMARY AND CONCLUSION

In this work, the application of fiber-based endoscopes (FBEs) in combustion and flow measurements has been investigated, especially for multidimensional and quantitative measurements. The use of FBEs circumvents the requirement for direct line-of-sight and facilitates the capture of multiple projection measurements on the same cameras. These unique features greatly reduce the implementation difficulty and cost of multidimensional measurements, especially in practical systems. However, the use of FBEs requires registering the locations and orientations of the FBEs carefully for quantitative measurements, and the spatial resolution of the images degrades after the images transmit through the FBEs. Hence this work focused on quantifying the accuracy of the view registration process and the spatial resolution degradation for FBEs.

Controlled experiments were performed to validate the view registration process and to test the resolving power of FBEs. The results show that, under the conditions tested in this work, the view registration process can be accurate within $\pm 0.5^\circ$ and the FBEs can resolve spatial features on the order of 0.25 mm. Such uncertainty in the view registration process and the spatial resolution both cause error in the interpretation of the images captured, which is reflected as the re-projection error. The work analyzed the re-projection error under conditions that were designed to make 3D measurements in a $1 \times 1 \times 1$ cm volume with a resolving power of ~ 0.3 mm, and found that the re-projection error was typically within ± 0.5 pixels.

Based on the understanding of the view registration process, the spatial resolution, and the re-projection error, demonstration experiments were performed to make instantaneous 3D measurements of flame structures at kHz temporal resolution. The measurements were made by performing a 3D tomographic inversion using projections captured by the FBEs as inputs. The

results demonstrate the FBEs' usefulness in implementing such 3D measurements, and their ability to resolve sub-millimeter flame features.

REFERENCES

1. R. S. Barlow, "Laser diagnostics and their interplay with computations to understand turbulent combustion " Proceedings of the Combustion Institute **31**, 49-75 (2007).
2. J. F. Driscoll, "Turbulent premixed combustion: Flamelet structure and its effect on turbulent burning velocities," Progress in Energy and Combustion Science **34**, 91-134 (2008).
3. S. T. Sanders, D. W. Mattison, L. Ma, J. B. Jeffries, and R. K. Hanson, "Wavelength-agile Diode-laser Sensing Strategies for Monitoring Gas Properties in Optically Harsh Flows: Application in Cesium-seeded Pulse Detonation Engine," Optics Express **10**, 505-514 (2002).
4. L. Ma, X. Li, S. T. Sanders, A. W. Caswell, S. Roy, D. H. Plemmons, and J. R. Gord, "50-kHz-rate 2D imaging of temperature and H₂/O concentration at the exhaust plane of a J85 engine using hyperspectral tomography," Optics Express **21**, 1152-1162 (2013).
5. V. Sick, "High speed imaging in fundamental and applied combustion research," Proceedings of the Combustion Institute **34**, 3509-3530 (2013).
6. R. Wellander, M. Richter, and M. Alden, "Time resolved, 3D imaging (4D) of two phase flow at a repetition rate of 1 kHz," Opt. Express **19**, 21508-21514 (2011).
7. M. R. Harker, T. Hattrell, M. Lawes, C. G. W. Sheppard, N. Tripathi, and R. Woolley, "Measurements of the Three-Dimensional Structure of Flames at Low Turbulence," Combustion Science and Technology **184**, 1818-1837 (2012).
8. J. Hult, A. Omrane, J. Nygren, C. F. Kaminski, B. Axelsson, R. Collin, P. E. Bengtsson, and M. Alden, "Quantitative three-dimensional imaging of soot volume fraction in turbulent non-premixed flames," Exp. Fluids **33**, 265-269 (2002).
9. W. Cai, X. Li, F. Li, and L. Ma, "Numerical and experimental validation of a three-dimensional combustion diagnostic based on tomographic chemiluminescence," Optics Express **21**, 7050-7064 (2013).
10. W. Cai, A. J. Wickersham, and L. Ma, "Three-Dimensional Combustion Diagnostics Based on Computed Tomography of Chemiluminescence," in 51st AIAA Aerospace Sciences Meeting Including the New Horizons Forum and Aerospace Exposition, (Dallas Region, TX, 2013).
11. J. Floyd, P. Geipel, and A. M. Kempf, "Computed Tomography of Chemiluminescence (CTC): Instantaneous 3D measurements and Phantom studies of a turbulent opposed jet flame," Combust. Flame **158**, 376-391 (2011).

12. J. Floyd and A. M. Kempf, "Computed Tomography of Chemiluminescence (CTC): High resolution and instantaneous 3-D measurements of a Matrix burner," *Proc. Combust. Inst.* **33**, 751-758 (2011).
13. F. Scarano, "Tomographic PIV: Principles and Practice," *Measurement Science & Technology* **24**(2013).
14. C. T. Herman, "Image Reconstruction from Projections" - The fundamentals of Computerized Tomography, *Computer Science and Applied Mathematics* (Academic Press, New York, USA, 1980).
15. K. D. Hinsch, "Holographic Particle Image Velocimetry," *Measurement Science & Technology* **13**, R61-R72 (2002).
16. L. Ma, "High Speed Imaging in Reactive Flows Using Hyperspectral Tomography and Photodissociation Spectroscopy," in *Laser Applications to Chemical, Security and Environmental Analysis*, (Optical Society of America, OSA Technical Digest Series, Paper LWA3, 2010),
17. X. Li and L. Ma, " Three-Dimensional Measurements of Turbulent Jet Flames at kHz Rate Based on Tomographic Chemiluminescence " in *AIAA SciTech 2014*, Paper AIAA-2014-0735, (National Harbor, MD, 2014).
18. X. An, T. Kraetschmer, K. Takami, S. T. Sanders, L. Ma, W. Cai, X. Li, S. Roy, and J. R. Gord, "Validation of Temperature Imaging by H₂O Absorption Spectroscopy Using Hyperspectral Tomography in Controlled Experiments," *Applied Optics* **50**, A29-A37 (2011).
19. N. Denisova, P. Tretyakov, and A. Tupikin, "Emission tomography in flame diagnostics," *Combustion and Flame* **160**, 577-588 (2013).
20. X. L. Weiwei Cai, and Lin Ma, "Practical Aspects of Implementing 3D Tomography Inversion for Volumetric Flame Imaging," *Applied Optics* **52**, in press. (2013).
21. J. Ballester and T. García-Armingol, "Diagnostic Techniques for the Monitoring and Control of Practical Flames," *Progress in Energy and Combustion Science*, **36**, 375-411 (2010).
22. H. Bheemul, G. Lu, and Y. Yan, "Three-Dimensional Visualization and Quantitative Characterization of Gaseous Flames," *Measurement Science and Technology*, **13**, 1643 (2002).

23. L. Ma, S. T. Sanders, J. B. Jeffries, and R. K. Hanson, "Monitoring and Control of a Pulse Detonation Engine Using a Diode-laser Fuel Concentration and Temperature Sensor," *Proceedings of the Combustion Institute* **29**, 161-166 (2002).
24. D. W. Mattison, C. M. Brophy, S. T. Sanders, L. Ma, K. M. Hinckley, J. B. Jeffries, and R. K. Hanson, "Pulse Detonation Engine Characterization and Control Using Tunable Diode-laser Sensors," *Journal of Propulsion and Power* **19**, 568-572 (2003).
25. O. Demuynck, O. Esteban, J. Lazaro, and D. Pizarro, "Non-Homogenous Illumination Correction of Calibrated Incoherent Optical-Fiber-Bundles for Image Transmission Purposes," in *Mechatronics, 2006 IEEE International Conference*, (IEEE, 2006), 150-153.
26. F. Li, X. Yu, H. Gu, Z. Li, Y. Zhao, L. Ma, L. Chen, and X. Chang, "Simultaneous Measurements of Multiple Flow Parameters for Scramjet Characterization Using Tunable Diode-laser Sensors," *Appl. Opt.* **50**, 6697-6707 (2012).
27. M. M. Hossain, G. Lu, and Y. Yan, "Three-dimensional reconstruction of combustion flames through optical fiber sensing and CCD imaging," in *Instrumentation and Measurement Technology Conference (I2MTC)*, (IEEE, 2011), 1-5.
28. R. Dils, "High-temperature optical fiber thermometer," *Journal of Applied Physics* **54**, 1198-1201 (1983).
29. O. Demuynck, "Optimized and quality improved incoherent optical fiber bundle calibration method for image transmission," *ISCGAV* **8**, 73-78 (2008).
30. M. Kang, X. Li, and L. Ma, "Calibration of Fiber Bundles for Flow and Combustion Measurements," in *AIAA SciTech 2014*, Paper AIAA-2014-0397, (National Harbor, MD, 2014).
31. V. N. Nori and J. M. Seitzman, "CH* Chemiluminescence Modeling for Combustion Diagnostics," *Proceedings of the Combustion Institute* **32**, 895-903 (2009).
32. Y. Hardalupas and M. Orain, "Local Measurements of the Time-Dependent Heat Release Rate and Equivalence Ratio using Chemiluminescent Emission from a Flame," *Combustion and Flame* **139**, 188-207 (2004).
33. C. N. Markides, G. De Paola, and E. Mastorakos, "Measurements and Simulations of Mixing and Autoignition of an n-Heptane Plume in a Turbulent Flow of Heated Air," *Experimental Thermal and Fluid Science* **31**, 393-401 (2007).

34. O. Stein, A. M. Kempf, and J. Janicka, "Les of the Sydney Swirl flame series: An initial investigation of the fluid dynamics," *Combustion Science and Technology* **179**, 173-189 (2007).
35. J.-Y. Bouguet, "Camera calibration toolbox for matlab," (2004).
36. J. Heikkila and O. Silven, "A four-step camera calibration procedure with implicit image correction," in *Proceedings of IEEE Computer Society Conference on Computer Vision and Pattern Recognition*, (IEEE, 1997), 1106-1112.
37. J. Floyd, "Computed Tomography of Chemiluminescence: A 3D Time Resolved Sensor for Turbulent Combustion," (Imperial College London, 2009).
38. Z. Zhang, "Flexible camera calibration by viewing a plane from unknown orientations," in *The Proceedings of the Seventh IEEE International Conference on Computer Vision*, (IEEE, 1999), 666-673.
39. D. C. Brown, "Decentering Distortion of Lenses," *Photogrammetric Engineering* **32**, 444-462 (1966).
40. D. C. Brown, "Close-range camera calibration," *Photogrammetric Engineering* **37**, 855-866 (1971).
41. X. Li and L. Ma, "Volumetric imaging of turbulent reactive flows at kHz based on computed tomography," *Optics Express* **22**, 4768-4778 (2014).
42. W. Cai, X. Li, and L. Ma, "Practical aspects of implementing three-dimensional tomography inversion for volumetric flame imaging," *Applied Optics* **52**, 8106-8116 (2013).
43. C. A. DiMarzio, *Optics for Engineers* (CRC Press Taylor & Francis Group, Boca Raton, FL, 2011).
44. W. Cai and L. Ma, "Comparison of Approaches Based on Optimization and Algebraic Iteration for Binary Tomography," *Computer Physics Communications* **181**, 1974-1981 (2010).
45. W. Cai and L. Ma, "Applications of Critical Temperature in Minimizing Functions of Continuous Variables With Simulated Annealing Algorithm," *Computer Physics Communications* **181**, 11-16 (2010).
46. X. Li and L. Ma, "Minimizing binary functions with simulated annealing algorithm with applications to binary tomography," *Computer Physics Communications* **183**, 309-315 (2012).

47. L. Ma, L. Kranendonk, W. Cai, Y. Zhao, and J. Baba, "Application of Simulated Annealing for Simultaneous Retrieval of Particle Size Distribution and Refractive Index,," *Journal of Aerosol Science* (2009).
48. L. Ma, W. Cai, A. W. Caswell, T. Kraetschmer, S. T. Sanders, S. Roy, and J. R. Gord, "Tomographic Imaging of Temperature and Chemical Species Based on Hyperspectral Absorption Spectroscopy," *Optics Express* **17**, 8602-8613 (2009).
49. L. Ma and W. Cai, "Numerical Investigation of Hyperspectral Tomography for Simultaneous Temperature and Concentration Imaging," *Applied Optics* **47**, 3751-3759 (2008).
50. C. K. Law, *Combustion Physics* (Cambridge University Press, New York, USA, 2006).
51. G. T. Herman, *Image Reconstruction from Projections: The Fundamentals of Computerized Tomography* (Academic Press, 1980).
52. J. Buckmaster, "A Mathematical Description of Open and Closed Flame Tips," *Combustion Science and Technology* **20**, 33-40 (1979).

APPENDIX A: DISTANCES AND ORIENTATIONS OF FBE INPUTS

Table 1. Distances and orientations of FBE inputs for premixed CH₄-O₂ cone-flame.

FBE Input	θ (°)	ϕ (°)	r (mm)
1	-59.0	89.5	139.7
2	-26.5	78.9	144.8
3	0.0	88.1	139.7
4	29.4	88.2	139.7
5	50.9	82.9	88.9
6	73.1	88.5	139.7
7	96.6	74.0	132.1
8	124.7	89.8	139.7
9	154.7	73.0	114.3
10	179.0	73.4	152.4

Table 2. Distances and orientations of FBE inputs for premixed CH₄-O₂ V-flame.

FBE Input	θ (°)	ϕ (°)	r (mm)
1	-49.0	0.0	220
2	-25.3	4.2	215
3	0.0	7.8	220
4	24.0	0.2	219
5	53.1	2.7	221
6	94.4	1.9	101
7	131.5	0.7	211
8	171.0	0.0	215
9	207.9	0.0	238
10	239.3	0.7	190

Table 3. Distances and orientations of FBE inputs for premixed C₃H₈-O₂ V-flame.

FBE Input	θ (°)	ϕ (°)	r (mm)
1	-109.1	0.0	215
2	-75.8	0.0	216
3	-36.7	0.0	211
4	0.0	0.0	219
5	37.8	0.0	221
6	73.2	0.0	217
7	114.0	0.0	211
8	152.1	0.0	215
9	163.8	20.5	238